Cyclin-G-associated kinase GAK/Aux orchestrates glial autophagy via Atg9 phosphorylation in Parkinson's disease

Shiping Zhang[1†], Linfang Wang[1†], Shuanglong Yi[1†], Shuhua Li[1], Honglei Wang[1], Li Song[2], Jiayao Ou[2], Min Zhang[1], Mengxiao Wang[1], Yuchen Zheng[1], Ruiqi Wang[1], Kai Yang[3], Tong Liu[4], Wei Yan[5], Chang Liu[5], Margaret S. Ho[1,*]

[1]School of Life Science and Technology, ShanghaiTech University, Shanghai, 201210, China

[2]Department of Anatomy and Neurobiology, Tongji University School of Medicine, Shanghai, 200092, China

[3]International Academic Center of Complex Systems, Advanced Institute of Natural Sciences, Beijing Normal University at Zhuhai 519087, China

[4]Institute of Neuroscience, State Key Laboratory of Neuroscience, CAS Center for Excellence in Brain Science and Intelligence Technology, Chinese Academy of Sciences, Shanghai 200031, China.

[5]Guangdong Provincial Key Laboratory of Brain Connectome and Behavior, CAS Key Laboratory of Brain Connectome and Manipulation, the Brain Cognition and Brain Disease Institute (BCBDI), Shenzhen Institutes of Advanced Technology, Chinese Academy of Sciences; Shenzhen-Hong Kong Institute of Brain Science-Shenzhen

Fundamental Research Institutions, Shenzhen, 518055, China.

[†]These authors contributed equally

[*]Corresponding author: Margaret S. Ho, Ph.D. Email: margareth@shanghaitech.edu.cn

Abstract

Glia serve as double-edged swords to modulate neuropathology in Parkinson's disease (PD), but how they react opposingly to be beneficial or detrimental under pathological conditions, like promote or eliminate α-Synuclein inclusions, remain elusive. Here we present evidence that the PD risk factor Cyclin G-associated kinase (GAK)/dAuxilin (Aux) is a new component in glial autophagy. Lack of GAK/Aux promotes autophagic induction, disrupts lysosome acidification, and blocks glial clearance of substrates. Aux regulates Atg9 trafficking to autophagosomes and lysosomes for autophagosome biogenesis and autolysosome maturation, respectively, via Atg9 phosphorylation at newly identified residues T62 and T69. GAK/Aux-mediated glial autophagy is required for α-Syn degradation and contributes to a broad spectrum of parkinsonian symptoms in *Drosophila* and mice. Our findings indicate that glial autophagy is a critical component in PD progression and identify a new autophagy factor functioning in a tissue-specific manner; targeting glial autophagy is potentially a therapeutic solution for PD.

Keywords: Autophagy; Glia; Parkinson's disease; *GAK*; *dauxilin*

Introduction

63 Aberrant protein trafficking, often associated with autophagy dysfunction, is one of the
64 major mechanisms underlying neurodegenerative diseases such as Parkinson's disease
65 (PD) (Menzies et al., 2017; Nixon, 2013). Three types of autophagy: microautophagy,
66 macroautophagy, and chaperone-mediated autophagy (CMA), have been described and
67 all lead to the final delivery of cargo to the lysosome for degradation and recycling. As
68 the primary catabolic mechanism, macroautophagy (henceforth referred to as
69 autophagy) was initially characterized as a bulk and non-selective degradation pathway
70 induced by nutrient deprivation. Constitutive autophagy at the basal level, however,
71 contributes to intracellular homeostasis in non-starved cells by degrading cellular
72 materials like damaged organelles or misfolded proteins (Galluzzi et al., 2017;
73 Mizushima, 2020). Interestingly, suppression of basal autophagy in the mouse nervous
74 system results in the accumulation of ubiquitinated proteins and neurodegeneration
75 (Hara et al., 2006; Komatsu et al., 2006), whereas enhancing basal autophagy in the
76 *Drosophila* nervous system promotes longevity and oxidant resistance (Simonsen et al.,
77 2008). Furthermore, disease-associated mutations in core autophagy genes have been
78 identified, supporting the link between autophagy and PD (Deng et al., 2017; Levine
79 and Kroemer, 2019). These findings mainly focus on a role for autophagy in neurons,
80 as perturbation of such process leads to catastrophic consequences including
81 pathological protein aggregation, deleterious lesions, and cell death (Kulkarni et al.,
82 2018). Intriguingly, autophagy function in the other brain cell type, glia, is less explored.
83 Whether glial autophagy is executed via similar interplay using the same components

84 as in neurons or other tissues, and whether it drives or contributes to neurodegeneration
85 in PD, remain largely unclear.

86 Glia serve as double-edged swords in PD via non-cell-autonomous mechanisms.
87 For instance, microglia secrete pro- or anti-inflammatory factors to enhance or
88 ameliorate PD progression (Gleichman and Carmichael, 2020; Ho, 2019;
89 Subhramanyam et al., 2019). Whereas α-Synuclein (α-Syn) accumulates in neurons,
90 evident α-Syn inclusions have been detected in microglia, astrocytes, and
91 oligodendrocytes due to prion-like propagation from neurons to glia (Dickson, 2012;
92 Jellinger, 2018; Peng et al., 2020; Sorrentino et al., 2019; Tanriover et al., 2020;
93 Valdinocci et al., 2017). Neuronally secreted α-Syn also impacts on these glial cells for
94 their reactivity and signaling to neurons (Cheng et al., 2018; Filippini et al., 2019).
95 These findings clearly demonstrate a pivotal role for glia in PD. Nonetheless, how the
96 α-Syn inclusions occur and persist in glia, and whether the regulatory mechanisms of
97 its elimination depends on glial autophagy, remain elusive.

98 Studies from yeast and mammals provided fundamental insights into *de novo*
99 autophagosome biogenesis mediated by the evolutionarily conserved autophagy-related
100 (ATG) genes (Galluzzi et al., 2017; Klionsky et al., 2016; Mizushima, 2020). Upon
101 autophagy initiation, stress induces the recruitment of ATG1/UNC-51 like kinase 1
102 (ULK1) complex to the phagophore assembly site or the pre-autophagosomal structure
103 (PAS). The ATG1/ULK1 complex facilitates the assembly of class III
104 phosphatidylinositol 3-kinase (PI3KC3) complex for PI3P production at the PAS, to

105 promote the nucleation of the isolated membranes (also termed phagophores) (Russell
106 et al., 2013). Whereas phagophore expansion is achieved by two ubiquitin-like
107 conjugation steps: the formation of ATG12-ATG5 conjugate and ATG8 lipidation,
108 additional lipids and proteins contributing to membrane expansion are delivered by the
109 ATG9-containing vesicles derived from the Golgi apparatus, recycling endosomes or
110 the plasma membrane (Mari et al., 2010; Orsi et al., 2012; Puri et al., 2014; Ravikumar
111 et al., 2010; Yamamoto et al., 2012). The expanded phagophores are sealed into a
112 double-layered autophagosome, which eventually fuses with lysosome to form
113 autolysosome, the milieu for degrading autophagic cargoes by acidic hydrolases.
114 Among all steps, very little is known about how the only transmembrane ATG protein
115 ATG9 contributes to autophagic induction and whether it plays additional roles in
116 autophagy. It is also not clear whether ATG9 functions in glial autophagy and
117 contributes to neurodegeneration.

118 Given these outstanding questions, we investigated the mechanism of glial
119 autophagy in PD. Here we present evidence that the PD risk factor Cyclin G-associated
120 kinase (GAK)/dAuxilin (Aux) functions in glial autophagy via Atg9 phosphorylation
121 at two newly identified threonine resides T62 and T69. In the absence of Aux, enhanced
122 Atg9 phosphorylation promotes its trafficking to autophagosomes and lysosomes to
123 increase autophagosome biogenesis and block autolysosome maturation, respectively.
124 Aux-mediated autophagic mechanism contributes to PD as lacking Aux causes a broad
125 spectrum of parkinsonian symptoms and blocks glial clearance of pathological

126 substrates including α-Syn. Consistently, lack of GAK induces microglial autophagy,
127 blocks α-Syn clearance, and leads to PD-like behaviors in mice. Taken together, our
128 findings identify a new player in glial autophagy and demonstrate the critical
129 requirement of glial autophagy in PD.
130
131 **Results**
132 ***GAK/aux* is expressed in glia**
133 Identified in a behavior screen, the *Drosophila* homolog of the PD risk factor GAK,
134 Aux, has been implicated in a broad spectrum of parkinsonian symptoms in a
135 *Drosophila* PD model (Song et al., 2017). GAK/Aux is a serine/threonine kinase that
136 regulates clathrin-uncoating, cell cycle progression, and hepatitis C entry (He et al.,
137 2020; Lee et al., 2006; Shimizu et al., 2009; Zhang et al., 2005). To investigate
138 GAK/Aux function in glia, GFP-labelled adult glia from flies expressing *UAS-*
139 *mCD8.GFP* under the control of the pan-glial driver *repo-GAL4* (*repo>mCD8.GFP*)
140 were first sorted by fluorescence-activated cell sorting (FACS) analysis. These sorted
141 glia exhibited high *repo* (a glial-specific marker) and low *elav* (a neuronal-specific
142 marker) expression, demonstrating their glial origin (Figures 1A and S1A). Interestingly,
143 *aux* was expressed in these sorted glia, with an expression level similar to the non-GFP
144 cells (Figure 1A). Consistent with the previously reported expression in microglia and
145 astrocytes (Zhang et al., 2014; Zhang et al., 2016), mammalian *GAK* expression was
146 also detected in the mouse immortalized microglia (IMG) cells stained positive for

147 ionized calcium-binding adapter molecule 1 (Iba1) or transmembrane protein 119
148 (TMEM119, Figures S1B, S1C, and S1G) (McCarthy et al., 2016). Treatment with
149 either of the two siRNAs targeting *GAK* reduced *GAK* expression in IMG cells as shown
150 by western blot (WB), RT-PCR, and immunostaining analyses (Figures S1D-S1H).
151 *GAK* mRNA and protein expression were also reduced in mouse microglia deficient of
152 *GAK* (*CX3CR1-Cre*$^{+/-}$*; GAK*$^{flox/flox}$) in the substantia nigra (SN, 36 weeks, Figures S1I-
153 S1K). Taken together, these results indicate that *GAK/aux* is expressed in adult fly glia
154 and mouse microglia.
155
156 **Aux regulates autophagosome formation in glia**
157 To investigate Aux function in glial autophagy, transgenic RNAi lines targeting *aux*
158 (V16182 and BL39017) were expressed in glia using *repo-GAL4*. RNAi expression
159 efficiently reduced *aux* expression as validated by RT-PCR, WB, and immunostaining
160 analyses (Figures S1L-S1O). Specific markers were used to label different autophagic
161 and endocytic organelles including Lamp1.GFP (lysosomes), mCherry.Atg8a
162 (autophagosomes), Rab7.GFP (late endosomes), and Rab5.GFP (early endosomes)
163 (Figure 1B). The morphology, distribution, and number of these endocytic and
164 autophagic organelles in glia were analyzed in different brain regions including the
165 region "Glia" enriched of glial processes, some glial nuclei, and most of the neuronal
166 nuclei, and the region "Antenna Lobe, AL" enriched of axon neuropils in close
167 proximity to glial processes (Figures 1C and 1D). Interestingly, downregulating *aux*

168 expression by *aux*-RNAi (V16182) caused a striking increase in the number of glial
169 Atg8a-positive autophagosomes (Figures 1E and 1F). These results, confirmed by one
170 additional *aux*-RNAi (*aux*-RNAi$^{\#2}$, BL39017), an endogenous protein trap *pmCh.Atg8a*,
171 anti-Atg8a antibodies, and *aux* mutant Mosaic Analysis with a Repressible Cell Marker
172 (MARCM) clones (Figures 1G, 1K, S2A, S2C, and S2E-S2H), indicate an increase in
173 glial autophagosome formation in the absence of glial Aux. Ultrastructural analysis by
174 Transmission Electron Microscopy (TEM) also showed an increase in the
175 autophagosome number upon *aux*-RNAi expression in glia (Figures 1H and 1L).
176 Furthermore, the intensities of microtubule-associated protein 1A/1B-light chain 3
177 (LC3) labeling autophagosomes and LC3-Iba1 colocalization increased in mouse
178 microglia deficient of *GAK*, indicating similar autophagosome defects (Figures 1I, 1M,
179 and 1N). Enlarged autophagosomes were also detected in *aux* mutant MARCM clones,
180 IMG cells treated with *GAK* siRNA, and mouse microglia deficient of *GAK* (Figures
181 1G, 1J, 1K, 1M, and 1O), further supporting the role of GAK/Aux in autophagosome
182 biogenesis. Notably, expression of *aux* or *hGAK* in glia suppressed the *aux*-RNAi-
183 induced increase in the autophagosome number (Figures 1P and 1Q). Taken together,
184 these results indicate that Aux regulates glial autophagosome formation and the
185 function of GAK/Aux is conserved across species.
186

187 **Lack of Aux causes lysosome aggregation in glia**

188 In addition to autophagosomes, the number, size, and AL fluorescent intensities of glial

189 Lamp1-positive lysosomes were increased in flies expressing *aux*-RNAi (Figures 2A-
190 2B, S2B, and S2D). Ultrastructural TEM analysis also showed an increase in the
191 number and size of lysosomes upon *aux*-RNAi expression in glia (Figures 2C and 2D),
192 further supporting our immunostaining results. Interestingly, glial Lamp1 fluorescent
193 signals exhibited dramatic increase and displayed as patches pronouncedly within the
194 AL near the neuropils (AL in Figures 2A and S2B), suggesting lysosome aggregation.
195 Similar lysosome aggregations were observed in IMG cells treated with the *GAK*
196 siRNA and mouse microglia deficient of *GAK* (Figures 2E-2H). *In-vivo* time lapse
197 analysis further demonstrated a reduction in the lysosome mobility, potentially leading
198 to aggregation (Figure S2I). Moreover, whereas Rab7-positive late endosomes also
199 aggregated (Figure S2J), the formation of the Rab5-positive early endosomes remained
200 largely unaffected (Figure S2K). Taken together, these results indicate that GAK/Aux
201 is required for glial autophagosome and lysosome formation; GAK/Aux is implicated
202 in glial autophagy, particularly at the steps of autophagosome biogenesis and terminal
203 lysosomal dynamics.
204

205 **Lack of Aux induces glial autophagy**

206 Based on an increase in the autophagosome number, it is conceivable that lack of glial
207 Aux induces or blocks autophagy. Interestingly, Atg8a/LC3 protein levels of samples
208 collected from adult fly heads or mouse IMG cells downregulating *aux* or *GAK*,
209 respectively, revealed an increase in the Atg8a-II/LC3-II protein levels, which further

210 increased in the presence of Bafilomycin A1 (BafA1), an inhibitor blocking lysosome
211 acidification and autophagosome-lysosome fusion (Mauvezin et al., 2015; Yoshimori
212 et al., 1991) (Figures 3A-3B and S3A). The levels of phosphorylated S6K (pS6K), a
213 downstream target of mTOR, also increased (Figures S3B and S3C). These results
214 suggest that lack of glial Aux induces autophagy. To further assess how the initiation of
215 glial autophagy is affected, phagophore nucleation and omegasome formation were
216 monitored using GFP markers labeling Atg6, Atg14, and ZFYVE. The number of
217 GFP.Atg6-, GFP.Atg14-, and GFP.ZFYVE-positive puncta were increased upon glial
218 *aux*-RNAi expression, indicating increased formation of autophagosome precursors
219 (Figures 3C-3F, S3D, and S3E). The size of GFP.ZFYVE-positive omegasomes were
220 significantly smaller, suggesting that these newly formed omegasomes might be
221 immature (Figures 3E and 3F). Taken together, these results indicate that autophagy is
222 induced in the absence of glial Aux; Aux suppresses glial autophagy.
223

224 **Glial Aux does not affect autophagosome-lysosome fusion**

225 To further demonstrate a role for Aux in glial autophagy, autophagic flux was analyzed
226 using a dual reporter *UAS-GFP-mCherry-Atg8a*. Whereas mCherry-positive puncta
227 were GFP-negative and autophagy proceeds normally in the control animals,
228 autophagic flux was impaired in the absence of glial Aux as the number of mCherry-
229 and GFP-positive puncta increased (Figures 3G and 3J). These puncta were abnormally
230 enlarged and exhibited non-quenched GFP signals, representing dysfunctional

231 autolysosomes that have already been fused but wrongly acidified. Consistently,
232 colocalization studies and Stimulated Emission Depletion (STED) imaging of
233 autophagosomes and lysosomes in adult fly glia expressing *aux*-RNAi revealed an
234 increased number of enlarged and well-colocalized autolysosomes, indicating that
235 abnormal autolysosomes are generated upon complete fusion (Figures 3H, 3I, 3K, and
236 3L). Ultrastructural TEM analysis also indicated an increase in the autolysosome
237 number upon glial *aux*-RNAi expression (Figures 3M and 3N). Taken together, these
238 results indicate that lacking glial Aux does not impair autophagosome-lysosome fusion,
239 as increasing number of autolysosomes are detected.

240 To further demonstrate that fusion is not affected, RNAi lines targeting fusion
241 factors such as *Syx17* or *vamp7* were expressed in the absence of glial Aux. Consistent
242 with previous findings, reducing *Syx17* or *vamp7* expression caused a block in fusion
243 (Hegedus et al., 2013), and co-expression of either RNAi reverted the *aux*-RNAi-
244 induced increase in Lamp1-Atg8a colocalization (Figures S3F-S3H). These results
245 suggest that autophagosomes and lysosomes fuse normally yet generate enlarged
246 autolysosomes in the absence of glial Aux; glial Aux suppresses autophagy while
247 autophagosome-lysosome fusion proceeds normally.

248

249 **Lack of Aux blocks autophagic substrate degradation by disrupting lysosome**
250 **acidification**

251 Despite a role in autophagic induction, inhibiting *aux* expression in glia caused

252 accumulation of autophagic substrates such as Ref(2)P, the *Drosophila* ortholog of P62,
253 and Ubiquitin (Ubi, Figures 4A-4D). P62 and Ubi were also accumulated in IMG cells
254 with downregulated *GAK* expression (Figures 4E-4H). These results suggest that
255 substrate degradation is blocked in these dysfunctional autolysosomes generated upon
256 glial GAK/Aux depletion.

257 Given that the block in substrate degradation is likely due to an unfavorable
258 environment in the enlarged and dysfunctional autolysosomes, Lysotracker dye was
259 used to analyze the acidification of labelled organelles in adult fly brains lacking glial
260 Aux. Interestingly, the Lysotracker intensities were significantly reduced in flies or
261 IMG cells downregulating glial *aux* or *GAK*, respectively, indicating that these
262 organelles are not properly acidified (Figures 4I-4J and S3I-S3J). Furthermore, the
263 activity of the lysosomal hydrolase cathepsin B (cathB) stained by Magic Red was
264 significantly lowered upon glial Aux depletion (Figures 4K and 4L). The processing of
265 the other lysosomal hydrolase cathepsin D (cathD) was also affected in the absence of
266 glial Aux, as the ratio of mature over total cathD was reduced (Figures 4M and 4N).
267 Taken together, these findings suggest that lack of Aux induces autophagy yet impairs
268 substrate degradation owing to insufficient lysosome acidification. Aux likely plays
269 dual roles in glial autophagy.

270

271 **Glial Aux regulates Atg9 phosphorylation**

272 To determine the mechanism of Aux in regulating glial autophagy, transgenic flies

273 expressing truncated Aux lacking each domain were created and validated by WB
274 analysis (Figures 5A and 5B). In contrast to *aux*-RNAi, overexpression of *aux* or its
275 truncated variants caused a decrease in the glial autophagosome number, indicating a
276 suppression effect on glial autophagy (Figures 5C and 5D). Expressing Aux lacking the
277 kinase domain ($Aux^{\Delta Kinase}$), however, caused significantly lower suppression on the
278 autophagosome number when comparing to Aux or other Aux variants, indicating that
279 Aux lacking the kinase domain is a less potent regulator in glial autophagy and the
280 kinase domain is important for Aux-mediated autophagic function.

281 Interestingly, phosphorylomic analysis on adult head samples collected from
282 control and *repo>aux*-RNAi flies revealed significant differences in the
283 phosphorylation profiles of autophagy-related proteins (Figures 5E and S4A).
284 Particularly, Atg9 (the fly homolog of mammalian ATG9) phosphorylation is
285 significantly upregulated at the threonine residues T62 and T69 upon glial Aux
286 depletion (Figure 5F). Probing the relationship between Aux and Atg9, *atg9* expression
287 in glia was first detected in sorted fly glia in a relatively high level compared to non-
288 glial cells (Figure 5G). Moreover, Atg9 colocalized with Aux in adult fly glia whereas
289 mouse ATG9 colocalized with GAK in IMG cells (Figures 5H and 5I). Both *atg9*
290 mRNA and protein levels were upregulated upon *aux*-RNAi expression in glia (Figures
291 5J-5L and S4B). These results demonstrate that Atg9 is a downstream target of glial
292 Aux.

293

294 **Glial Aux regulates autophagic induction via Atg9 phosphorylation**

295 Next, we determine if Aux-mediated glial autophagic induction depends on Atg9 and
296 its phosphorylation. Whereas inhibiting *atg9* expression in glia caused a decrease in the
297 number of omegasomes and autophagosomes (Figures 6A-6B and S4C-S4D), co-
298 expression of *atg9*-RNAi suppressed the *aux*-RNAi-induced increase in the glial
299 autophagosome number (Figures S4C and S4D). These results indicate that Atg9
300 functions downstream of Aux in regulating glial autophagosome biogenesis and
301 autophagic induction. Similarly as *aux*-RNAi, the expression of Atg9 or
302 phosphomimetic Atg9 mutants with the two threonine residues mutated to glutamate
303 ($Atg9^{T62E}$, $Atg9^{T69E}$, or double mutant $Atg9^{T62E-T69E}$) increased the number of
304 omegasomes and autophagosomes, while the expression of non-phosphorylatable Atg9
305 mutants with the two threonine residues mutated to alanine ($Atg9^{T62A}$, $Atg9^{T69A}$, or
306 double mutant $Atg9^{T62A-T69A}$) inhibited omegasome and autophagosome information
307 (Figures 6C-6D and S4E-S4F). These results suggest that Atg9 phosphorylation at T62
308 and T69 is required for autophagosome biogenesis and autophagic induction in glia.
309 Notably, co-expression of either of the three non-phosphorylatable Atg9 mutants
310 suppressed the *aux*-RNAi-induced increase in omegasome and autophagosome
311 formation (Figures 6E and S4G), demonstrating that glial Aux regulates
312 autophagosome biogenesis and autophagic induction via Atg9 phosphorylation.

313

314 **Glial Aux regulates Atg9 trafficking to autophagosomes in a phosphorylation-**

315 **dependent manner**

316 To further dissect how glial Aux regulates autophagic induction via Atg9, Atg9
317 trafficking to autophagosomes was analyzed. Reducing *aux* expression in glia increased
318 the colocalization of Atg9 and Atg8a-positive autophagosomes, suggesting that lack of
319 Aux promotes Atg9 trafficking to autophagosomes (Figures 6F and 6G). Given that
320 Atg9 phosphorylation on T62 and T629 is enhanced in the absence of glial Aux,
321 phosphomimetic Atg9 mutants were tested for their effects on trafficking. Similarly,
322 expressing either of the three phosphomimetic Atg9 mutants in glia increased the Atg9
323 colocalization with autophagosomes, indicating that Atg9 phosphorylation promotes its
324 trafficking (Figure 6H). Co-expression of either of the three non-phosphorylatable Atg9
325 mutants also suppressed the *aux*-RNAi-induced increase in Atg9-Atg8a colocalization
326 (Figure 6I), further demonstrating a role for Atg9 phosphorylation in Aux-mediated
327 Atg9 trafficking, followed by autophagic induction. Taken together, these results
328 indicate that Atg9 acts downstream of Aux in regulating the induction of glial
329 autophagy; Aux promotes Atg9 trafficking in a phosphorylation-dependent manner.

330

331 **Glial Aux regulates autolysosome maturation via Atg9 phosphorylation**

332 In addition to autophagosomes, a portion of Atg9 was found to be transported to
333 lysosomes upon glia Aux depletion, indicating that Atg9 might also play a role in Aux-
334 mediated lysosome acidification (Figure 6J). Interestingly, inhibiting *atg9* expression
335 in glia caused a decrease in the intensities of Lysotracker-positive puncta (Figures 6K

336 and 6L). In contrast to *aux*-RNAi, expression of Atg9 or either of the three non-
337 phosphorylatable Atg9 mutants enhanced the Lysotracker intensities (Figures 6M and
338 6N). Co-expression of either of the three Atg9 mutants also restored the *aux*-RNAi-
339 induced reduction in the Lysotracker intensities (Figure 6O). Altogether, these results
340 indicate that Atg9 acts downstream of Aux to mediate lysosome acidification; Atg9
341 phosphorylation is critical in establishing a proper pH gradient in lysosomes for
342 autolysosomal degradation.
343
344 **Glia Aux contributes to PD-like symptoms**
345 To investigate whether Aux-mediated glial autophagy contributes to PD, a broad
346 spectrum of PD-like behaviors were analyzed upon glial Aux depletion. Interestingly,
347 lacking glial Aux caused significant loss of PPM1/2 DA neurons, disrupted locomotor
348 function, and shorten fly lifespan in an age-dependent manner (Figures 7A-7E). Some
349 of the earlier PD-associated symptoms such as sleep defects were also detected upon
350 glial Aux depletion (Figures S5A and S5B). Similar DA neuron loss and locomotor
351 defects, in addition to body weight loss and impaired movement in the pole test, were
352 also seen in mice lacking microglial *GAK* (Figures 7F-7I and S5C). Furthermore, using
353 a genetic binary system, human α-Syn was selectively expressed in fly neurons while
354 abolishing *aux* expression in glia. Not only that total α-Syn protein levels increased
355 upon glial Aux depletion (Figures 7L and 7M), α-Syn proteins were also detected in
356 sorted fly glia, despite its neuronal origin (Figure S5D). These results indicate that α-

357 Syn transmits from neurons to glia and accumulates in the absence of glial Aux.
358 Whereas mouse microglia lacking *GAK* exhibited significantly shorter processes in a
359 potentially activated state (Figures 7J and 7N), α-Syn levels were also elevated in these
360 *GAK*-deficient microglia (Figures 7K and 7N). In addition, accumulated α-Syn
361 exhibited increased colocalization with Lamp1 or LC3 in microglia deficient of *GAK*,
362 suggesting that α-Syn degradation by autophagy in these microglia is blocked (Figures
363 5E-5I). Taken together, GAK/Aux-mediated glial autophagy is pathologically relevant
364 and targets α-Syn for degradation during PD progression.
365

366 **Discussion**

367 **Glial autophagy vs. neuronal autophagy**

368 Neuronal autophagy has been considered as one of the major mechanisms underlying
369 PD. More is known about how autophagosomes are formed *de novo* at the axon
370 terminals to traffic back to soma where lysosomes are abundant, and how
371 autolysosomes are generated to degrade unwanted organelles or proteins once
372 efficiently fused (Cheng et al., 2015; Maday et al., 2012). This mechanism is useful
373 under the pathological condition when target proteins start to accumulate.
374 Dysfunctional neuronal autophagy, thus, aggravates pathological consequences.
375 Although autophagy components and mechanisms might be universal among all tissues,
376 it remains unclear how autophagy in glia is operated. Our findings indicate that most of
377 the *atg* genes are expressed in glia in similar or potentially higher levels compared to

378 neurons (Figure 6A). Silencing their expression selectively in glia, leading to the block
379 of glial autophagy, results in locomotor abnormalities and DA neurodegeneration,
380 suggesting that *atg* gene expression in glia might act in similar means as in neurons and
381 are equally important for PD-like behaviors and DA neuron survival (Figures 6B-6D).
382 In addition, a recent study also uncovers dysfunctional glial autophagy linking to
383 abnormal α-Syn degradation in microglial *Atg7* knockout mice (Choi et al., 2020).
384 Findings in the present study further demonstrate the importance of glial autophagy,
385 yet it remains unclear how neuronal and glial autophagy differ and how glial autophagy
386 contributes to neurodegeneration in PD. It is noteworthy to mention that the overall
387 morphology or distribution of lysosomes and autophagosomes remains largely intact
388 upon reducing *aux* expression pan-neuronally (Figure S7). These results suggest that
389 Aux functions separately in neurons vs. glia, implicating differential requirement of
390 glial autophagy vs. neuronal autophagy in PD.
391
392 **GAK/Aux is a new player in glial autophagy**
393 We identify GAK/Aux as a new component in glial autophagy. Aux regulates glial
394 autophagy via Atg9 phosphorylation, hence the trafficking of membrane sources to
395 orchestrate autophagosome biogenesis and autophagic induction. On the other hand,
396 Aux-mediated Atg9 activity also regulates autolysosome maturation by mediating
397 lysosomal acidification to develop a properly acidic environment for degradation.
398 These combined activities ultimately coordinate autophagy function in glia. In addition

399 to its role in autophagic induction, Atg9 has also been reported to function in
400 intraluminal vesicle formation and compartmentalized acidification within amphisomes
401 and autolysosomes (Bader et al., 2015). As the only integral membrane protein in the
402 core autophagy machineries, Atg9 might regulate amphisome/autolysosome activity by
403 providing membrane sources to form the intraluminal vesicles required for proper
404 lysosome acidification similarly as providing membrane sources to PAS for
405 autophagosome biogenesis. Intriguingly, our findings pinpoint a role of Atg9
406 phosphorylation in these processes. Whereas Aux plays a role in regulating Atg9
407 phosphorylation, enhanced Atg9 phosphorylation upon glial Aux depletion promotes
408 its transport to autophagosomes or lysosomes to regulate autophagosome biogenesis or
409 autolysosome maturation, respectively.

410 Atg9 phosphorylation at different residues has been reported in promoting its
411 anterograde trafficking to initiate autophagy (Feng et al., 2016; Zhou et al., 2017).
412 Mammalian Src and ULK1 kinases phosphorylate mATG9 N-terminus at Y8 and S14,
413 respectively, to enhance mATG9 interaction with the adaptor protein AP1 complex,
414 promoting mATG9 trafficking from the plasma membrane to initiate autophagy (Zhou
415 et al., 2017). Yeast Atg1 also phosphorylates Atg9 C-terminus to recruit Atg18 to the
416 PAS for autophagosome membrane expansion (Papinski et al., 2014). Interestingly, our
417 results show that Atg9 phosphorylation at the N-terminus T62 or T69 promotes its
418 colocalization with Atg8a and omegasome formation, indicating a role in autophagic
419 induction. Once phosphorylated, similar mechanisms might be employed to enhance

420 Atg9 interaction with AP1/2 complex or Atg18 to promote autophagy.

421 Given that Atg1-mediated Atg9 phosphorylation is crucial for Atg9 trafficking and
422 autophagic induction, we tested whether Aux interacts with Atg1. Co-
423 immunoprecipitation analysis indicated that Aux physically interacts with Atg1,
424 suggesting that Aux might act via Atg1 to regulate Atg9 phosphorylation at T62 and
425 T69 (Figure S8). It has been shown that mTOR senses the nutrient-rich condition and
426 blocks autophagic induction by phosphorylating mammalian ULK1 at S757 to prevent
427 its activation (Kim et al., 2011). Similarly, GAK/Aux might also act as a sensor, but to
428 sense pathological signals, to prevent Atg1 activation and autophagic induction by
429 modulating Atg1-mediated Atg9 phosphorylation.

430 On the other hand, it is also possible that GAK/Aux mediates glial autophagy via
431 its interaction with the AP1/2 adaptor complexs in clathrin-mediated trafficking.
432 GAK/Aux might phosphorylate AP1/2 to enhance its interaction with Atg9, thereby
433 promote Atg9 trafficking and autophagic initiation, whereas Atg9 phosphorylation
434 might be a secondary consequence upon glial Aux depletion. Nonetheless, our findings
435 indicate that earlier Rab5-mediated endocytic traffics are not affected by glial Aux
436 depletion (Figure S2K). Aux lacking the clathrin-uncoating activity also does not affect
437 glial autophagy (Figures 5C and 5D). Furthermore, general inhibition of clathrin-
438 mediated internalization decreases autophagosome biogenesis (Puri et al., 2013;
439 Ravikumar et al., 2010). Based on these findings, it is unlikely that Aux regulates glial
440 autophagy via its uncoating function, as lack of Aux induces rather than suppresses

441 glial autophagy.

442

443 **Aux-mediated glial autophagy functions in α-Syn clearance**

444 Unlike neurons, glia are not polarized, despite the terminal processes are often in close
445 proximity to axon neuropils. The intimate interaction between glia and axons suggest a
446 possible function for glial autophagy in mediating degradation of substances
447 transmitted from neurons. For instance, autolysosomes at the terminal glial processes
448 are readily available for degrading neuronal α-Syn, whereas axonal autophagosomes
449 have to travel back to soma to generate autolysosome for degradation. Given the
450 relative positions, it seems likely that glial autophagy is a more energy efficient route
451 compared to neuronal autophagy when degrading substrates under pathological
452 conditions. Despite the benefits of inducing glial autophagy, lack of GAK/Aux also
453 disrupts lysosome acidification and blocks substrate degradation. Owing to its dual
454 roles, the attempt to initiate the glial clearance program ultimately failed, leading to α-
455 Syn accumulation, a block in further transmission, and neurodegeneration in PD.
456 Considering that prominent inclusions of α-Syn have been detected in astrocytes,
457 microglia, and oligodendrocytes (Dickson, 2012; Tanriover et al., 2020), identified
458 GAK SNPs might cause reduced *GAK* expression in PD, then critically controls the
459 onset of glial autophagy to allow α-Syn either propagates from cell to cell in a prion-
460 like fashion, locally accumulates due to a failure in autophagic substrate degradation,
461 or to be eliminated by the induction of glial autophagy.

462

463 **Aux-mediated glial autophagy contributes to PD**

464 As most of the hypotheses that underlie PD pathology are often driven by a neuronal
465 origin of dysfunctional machineries or cellular defects, glia have only recently been
466 purposed as possible drivers for neurodegeneration (Gleichman and Carmichael, 2020).
467 For instance, the Alzheimer's disease (AD) risk factor gene *Apolipoprotein E* (*APOE*)
468 is predominantly expressed in astrocytes (Xu et al., 2006) and its genetic mutations are
469 associated with an increasing risk of developing AD, supporting a role for genetic
470 causes from glia driving neurodegeneration. Here we add to the list a PD risk factor of
471 glial origin in modulating PD pathology. Although the relationship between GAK
472 deficiency and PD is still uncertain, lacking glial GAK/Aux leads to a broad spectrum
473 of parkinsonian symptoms in both *Drosophila* and mice. These include dysfunctional
474 locomotor activity, DA neurodegeneration, and some of the earlier symptoms such as
475 sleep defects. As an identified Aux downstream target, glial Atg9 depletion also causes
476 similar defects in autophagy and PD-like behaviors. Considering the role of glia as a
477 double-edged sword in PD, the seemingly contradictory roles of GAK/Aux in
478 autophagosome biogenesis and autolysosome maturation might independently
479 dominate at different period of time, leading to differential glial responses that
480 aggravate or ameliorate the disease progression. These findings provide new insights
481 on PD pathology from a glial perspective and elucidate the mechanism of glial
482 autophagy. Future work will be required to investigate how GAK/Aux plays different

483 roles in glia and neurons, and how it contributes to neurodegeneration in a tissue-
484 specific manner.
485

486 **Acknowledgments**

487 We thank Bloomington *Drosophila* Stock Center, Vienna *Drosophila* RNAi Center,
488 Tsinghua Fly Center, the Core Facility of *Drosophila* Resource and Technology,
489 Shanghai Institute of Biochemistry and Cell Biology, Chinese Academy of Sciences,
490 Developmental Studies Hybridoma Bank, Chao Tong, Henry C. Chang, Lei Xue, Henry
491 Sun, Tor Erik Rusten, Gabor Juhasz, Patrik Verstreken, Aike Guo, Yijun Liu, and
492 Gerald M Rubin for fly stocks and antibodies; Chih-Hao Lee for IMG cell line; Jiawei
493 Zhou for *CX3CR1-Cre* mice. We also thank the Molecular Imaging Core Facility
494 (MICF), the Molecular and Cell Biology Core Facility (MCBCF), and the Multi-Omics
495 Core Facility (MOCF) at the School of Life Science and Technology, ShanghaiTech
496 University for providing technical support; Yu Kong and Lijun Pan in Electron
497 Microscopy Facilities of Center for Excellence in Brain Science and Technology,
498 Chinese Academy of Science for assistance with EM sample preparation; Wei-Chung
499 Lee for help on EM; Ho lab members for discussion and comments. This work was
500 supported by grants from ShanghaiTech, National Natural Science Foundation of China
501 (31871039, 32071009), Natural Science Foundation of Guangdong Province
502 (2020A1515011055), and Shenzhen Key Laboratory of Drug Addiction
503 (ZDSYS20190902093601675).

504

505 **Author contributions**

506 S.Z, L.W, S.Y, and M.S.H conceived and designed the study. S.Z, L.W, S.Y, S.L, H.W,
507 L.S, J.O, M.Z, M.W, Y.Z, R.W, K.Y, T.L, W.Y, and M.S.H performed the experiments.
508 S.Z, L.W, S.Y, S.L, C.L, and M.S.H analyzed the data. M.S.H wrote the paper with the
509 input of S.Z, L.W, S.Y, and S.L. All authors read and approved the manuscript.

510

511 **Declaration of Interests**

512 The authors declare no competing interests.

513

514 **Figure Legends**

515 **Figure 1. Aux regulates autophagosome formation in glia** (**A**) Gene expression was
516 analyzed in GFP-positive adult glia sorted by FACS analysis from flies expressing
517 *UAS-mCD8.GFP* under the control of *repo-GAL4* (*repo-GAL4>UAS-mCD8.GFP*).
518 Note that GFP-sorted glia exhibit high *repo* and low *elav* expression. *aux* is expressed
519 in both neurons and glia. (**B**) Schematic diagram on endocytic and autophagic
520 trafficking. Markers used to label different organelles include: Rab5.GFP for early
521 endosomes, Rab7.GFP for late endosomes, Lamp1.GFP for lysosomes, and
522 mCherry.Atg8a for autophagosomes. (**C** and **D**) Illustration (C) and representative
523 images (D) of an adult fly brain with the olfactory associative center mushroom body
524 (MB), antenna lobe (AL), and the gustatory suboganglion (SOG). Dashed squares in

525 yellow and blue indicate the regions "Glia" enriched with GFP- and Repo-positive glia
526 (green and magenta) and "AL" enriched with axon neuropils. Neuronal nuclei are Elav-
527 positive (red). (**E** and **F**) Representative images (E) and quantifications (F) of glial
528 autophagosomes in the Whole brain, Glia, and AL. Autophagosomes (red) are labeled
529 with *repo-GAL4* driven *UAS-mCherry.Atg8a*. Note that downregulating glial *aux*
530 induces an increase in the autophagosome number in both regions Glia and AL. (**G** and
531 **K**) Glial MARCM clones of *aux* mutants (aux^{L78H}, aux^{G257E}, and aux^{I670K}) expressing
532 *UAS-mCh.Atg8a* by *repo-GAL4*. Note that the number and size of glial autophagosomes
533 per clone increase in *aux* mutants. (**H** and **L**) Representative TEM images (H) and
534 quantifications (L) of autophagosomes in the control and *repo>aux*-RNAi adult fly
535 brains. Note an increase in the number of autophagosomes (pink asterisks) when *aux*-
536 RNAi is expressed in glia. (**I**,**M**,**N**) Representative images (I) and quantifications (M
537 and N) of LC3-positive autophagosomes in mouse substantia nigra (SN) microglia
538 deficient of *GAK* (*CX3CR1-Cre*$^{+/-}$; *GAK*$^{flox/flox}$) at 36 weeks. Note the intensities and
539 size of LC3-positive autophagosomes and the LC3-Iba1 colocalization increase upon
540 microglial GAK depletion. (**J** and **O**) Representative images (J) and quantifications (O)
541 of LC3-positive autophagosomes in IMG cells treated with the *GAK* siRNA. Note that
542 LC3-positive autophagosomes are enlarged upon abolishing *GAK* expression. (**P** and
543 **Q**) Co-expression of fly *aux* or human *GAK* (*hGAK*) suppresses the *aux*-RNAi-induced
544 increase in glial autophagosome number. Scale bars and the numbers of brains
545 quantified are indicated in the Figures. For TEM, more than 40 images from at least 5

546 independent fly brains of each genotype were analyzed. Data are shown as mean ± SEM.
547 P-values of significance (indicated with asterisks, ns no significance, * $p<0.05$, **
548 $p<0.01$, and *** $p<0.001$) are calculated by two-tailed unpaired t-test or ordinary one-
549 way ANOVA followed by Tukey's multiple comparisons test. Approximately 30
550 confocal Z-stack sections were taken with 0.4 μm each, and representative single layer
551 images acquired at the similar plane of brains across all genotypes are shown. Pearson's
552 R values for colocalization are calculated based on methods described. Quantification
553 figures from the same image but with different parameters quantified are shown under
554 the same label. All genotypes analyzed are included in Key Resources Table. All data
555 in subsequent Figures are present and analyzed as described in Figure 1 unless stated
556 otherwise.
557
558 **Figure 2. Lack of glial Aux induces lysosome aggregation** (**A** and **B**) Representative
559 images (A) and quantifications (B) of glial lysosomes in the Whole brain, Glia, and AL.
560 Lysosomes (green) are labeled with *repo-GAL4* driven *UAS-Lamp1.GFP*. Note that
561 downregulating glial *aux* induces an increase in the lysosome number and size in Glia
562 region and lysosome fluorescent intensities in AL. (**C** and **D**) Representative TEM
563 images (D) and quantifications (C) of lysosomes in the control and *repo>aux*-RNAi
564 adult fly brains. Note an increase in the number and size of lysosomes (yellow arrows)
565 with the presence of large lysosome-like structures (red arrows) when *aux*-RNAi is
566 expressed in glia. (**E** and **F**) Representative images (E) and quantifications (F) of

567 Lamp1-positive lysosomes in IMG cells treated with the *GAK* siRNA. Note that
568 Lamp1-positive lysosome intensities increase upon abolishing *GAK* expression. (**G** and
569 **H**) Representative images (G) and quantifications (H) of Lamp1-positive lysosomes in
570 mouse SN microglia deficient of *GAK* (*CX3CR1-Cre*$^{+/-}$; *GAK*$^{flox/flox}$) at 36 weeks. Note
571 the Lamp1-positive intensities and the Lamp1-Iba1 colocalization increase upon
572 microglial GAK depletion. Scale bars and the numbers of brains quantified are
573 indicated in the Figures. Data are shown as mean ± SEM. P-values of significance
574 (indicated with asterisks, ns no significance, * $p<0.05$, ** $p<0.01$, and *** $p<0.001$)
575 are calculated by two-tailed unpaired t-test or ordinary one-way ANOVA followed by
576 Tukey's multiple comparisons test.
577
578 **Figure 3. Lack of glial Aux induces autophagy but does not impair**
579 **autophagosome-lysosome fusion** (**A** and **B**) Representative WB images (A) and
580 quantifications (B) of Atg8a-I and II protein levels in the control and *repo>aux*-RNAi
581 adult fly brains. Note that lack of glial Aux increases both Atg8a-I and II protein levels,
582 which further increases in the presence of BafA1. More than three independent
583 replicates are analyzed. (**C** to **F**) Representative images (C and E) and quantifications
584 (D and F) of GFP-positive puncta labeling phagophore nucleation (*repo>UAS-*
585 *GFP.Atg6*) and omegasome formation (*repo>UAS-GFP.ZFYVE*) in adult fly glia with
586 the indicated genotypes. Note that glial Aux depletion induces phagophore nucleation
587 and omegasome formation in glia. (**G** and **J**) Autophagic flux is impaired as examined
588 by expressing the flux reporter *UAS-GFP-mCh-Atg8a* in adult fly glia. Note that GFP-

589 and mCh-positive autolysosomes are enlarged and potentially dysfunctional as shown
590 by the non-quenched GFP signals. (**H**,**I**,**K**,**L**) Representative confocal/STED images (H
591 and I) and quantifications (K and L) of Lamp1- and Atg8a-positive puncta in adult fly
592 brains with the indicated genotypes. Note that Aux depletion in glia increases the
593 number and size of glial autolysosomes and the colocalization of autophagosomes and
594 lysosomes. (**M** and **N**) Representative TEM images (M) and quantifications (N) of
595 autolysosomes in the control and *repo>aux*-RNAi adult fly brains. Note an increase in
596 the number of autolysosomes (blue arrows) when *aux*-RNAi is expressed in glia. Scale
597 bars and the numbers of brains quantified are indicated in the Figures. Data are shown
598 as mean ± SEM. P-values of significance (indicated with asterisks, ns no significance,
599 * $p<0.05$, ** $p<0.01$, and *** $p<0.001$) are calculated by two-tailed unpaired t-test or
600 ordinary one-way ANOVA followed by Tukey's multiple comparisons test.
601
602 **Figure 4. Lack of glial Aux blocks autophagic substrate degradation by disrupting**
603 **lysosome acidification** (**A-D**) Autophagic substrates such as Ref(2)P and Ubiquitin
604 (Ubi) accumulate in *repo>aux*-RNAi adult fly brains as revealed by immunostaining
605 and WB analyses. (**E-H**) WB analyses reveal an increase in P62 (E and F) and Ubi (G
606 and H) protein levels upon GAK depletion in IMG cells. **(I-L**) The number and
607 fluorescent intensities of Lysotracker Green- (I and J) or Magic Red-positive (K and L)
608 puncta decrease upon glial Aux depletion. (**M** and **N**) The processing of the lysosomal
609 protease cathD is analyzed by WB analysis. Note that lacking glial Aux alters cathD

610 processing and the ratio of mature over total cathD levels decreases. More than three
611 independent replicates are analyzed for WB analysis. Scale bars and the numbers of
612 brains quantified are indicated in the Figures. Data are shown as mean ± SEM. P-values
613 of significance (indicated with asterisks, ns no significance, * $p<0.05$, ** $p<0.01$, and
614 *** $p<0.001$) are calculated by two-tailed unpaired t-test or ordinary one-way ANOVA
615 followed by Tukey's multiple comparisons test.
616
617 **Figure 5. Atg9 is a downstream target of glial Aux** (**A** and **B**) Schematic diagram of
618 Aux protein domains and expression of different Aux protein variants by WB analysis.
619 (**C** and **D**) Representative images (C) and quantifications (D) of glial autophagosome
620 number in adult fly brains expressing Aux variants lacking different domains. Note that
621 autophagosome number is reduced when expressing different variants, with Aux
622 lacking the kinase domain exhibit a less potent effect. (**E**) Phosphorylomic analysis of
623 adult fly brains from control and *repo>aux-RNAi* animals. Note that phosphorylation
624 of various Atg proteins is greatly altered upon glial Aux depletion. (**F**) Atg9
625 phosphorylation on two threonine residues T62 and T69 is enhanced by glial Aux
626 depletion. (**G**) *atg9* is expressed in GFP-positive adult fly glia sorted by FACS analysis.
627 (**H** and **I**) Mouse ATG9 colocalizes with GAK while the fly Atg9 colocalizes with Aux
628 in IMG cells and adult fly brains, respectively. *EGFP-Atg9* transgenic flies were used
629 for colocalization analysis. (**J-L**) Both *atg9* mRNA (L) and protein levels (J and K)
630 increase in adult fly brains upon glial Aux depletion. *atg9* mRNA levels were analyzed

631 in glia sorted by FACS analysis. More than three independent replicates are analyzed
632 for WB analysis. Scale bars and the numbers of brains quantified are indicated in the
633 Figures. Data are shown as mean ± SEM. P-values of significance (indicated with
634 asterisks, ns no significance, * $p<0.05$, ** $p<0.01$, and *** $p<0.001$) are calculated by
635 two-tailed unpaired t-test or ordinary one-way ANOVA followed by Tukey's multiple
636 comparisons test.
637
638 **Figure 6. Aux regulates autophagic induction and autolysosome maturation via**
639 **Atg9 phosphorylation** (**A-E**) Representative images (A and C) and quantifications
640 (B,D,E) of glial GFP.ZFYVE-positive omegasomes in brains with the indicated
641 genotypes. Note that the expression of *atg9*-RNAi or the non-phosphorylatable
642 $Atg9^{T62A}$ or $Atg9^{T62A-T69A}$ mutants reduces while the expression of Atg9 or the
643 phophomimetic $Atg9^{T69E}$ or $Atg9^{T62E-T69E}$ increases the glial omegasome number. Co-
644 expression of either of the three non-phosphorylatable Atg9 mutants suppresses the
645 *aux*-RNAi-induced increase in the glial omegasome number (E). (**F-I**) Representative
646 images (F) and quantifications (G-I) of Atg9-Atg8a colocalization in adult fly glia with
647 the indicated genotypes. Note that the expression of *aux*-RNAi or either of the three
648 phophomimetic Atg9 mutants promotes Atg9 trafficking to autophagosomes. Co-
649 expression of either of the three non-phosphorylatable Atg9 mutants suppresses the
650 *aux*-RNAi-induced increase in Atg9-Atg8a colocalization. (**J**) The colocalization of
651 Atg9- and Lamp1-positive lysosomes is also increased upon glial Aux depletion. (**K-O**)

652 Representative images (K and M) and quantifications (L,N,O) of Lysotracker intensities
653 and puncta number in adult fly brains with the indicated genotypes. Note that the
654 expression of *atg9*-RNAi or *aux*-RNAi decreases the intensities and number of
655 Lysotracker-positive puncta, while the expression of either of the three non-
656 phosphorylatable Atg9 mutants results in the opposite. Expressing either of the three
657 non-phosphorylatable Atg9 mutants restores the *aux*-RNAi-induced reduction in the
658 Lysotracker intensities. All transgenic flies expressing Atg9 or its variants were made
659 with a N-terminal 3XHA tag for protein detection. Scale bars and the numbers of brains
660 quantified are indicated in the Figures. Data are shown as mean ± SEM. P-values of
661 significance (indicated with asterisks, ns no significance, * $p<0.05$, ** $p<0.01$, and ***
662 $p<0.001$) are calculated by two-tailed unpaired t-test or ordinary one-way ANOVA
663 followed by Tukey's multiple comparisons test.
664
665 **Figure 7. Glial GAK/Aux contributes to PD-like symptoms** (**A**) Illustration of an
666 adult fly brain with different DA neuron clusters. The selected areas with PPM1/2
667 clusters are enclosed by the red dashes, enlarged below the illustration, and visualized
668 in B. (**B** and **C**) Representative images (B) and quantifications (C) of DA neuron
669 number in the adult fly brains with the indicated genotypes. Note that DA neuron
670 number in the PPM1/2 cluster decreases in an age-dependent manner. (**D** and **E**) Fly
671 locomotor activity and lifespan are disrupted upon glial Aux depletion. (**F** and **G**) DA
672 neuron number in SN decreases in mice deficient of microglial *GAK* at 36 weeks. (**H**

673 and **I**) Footprint analysis and pole test of mice deficient of microglial *GAK*. Note that
674 the locomotor activity of these mice is apparently disrupted starting at 21 weeks. (**J**,**K**,**N**)
675 Representative images (N) and quantifications (J and K) of α-Syn intensities in Iba1-
676 positive microglia deficient of *GAK* at 21 weeks. Note that *GAK*-deficient microglia
677 exhibit significantly shorter processes, amoeboid-like structures, and increased α-Syn
678 intensities. (**L** and **M**) Representative images (L) and quantifications (M) of α-Syn
679 intensities (green) in adult fly brains expressing *aux*-RNAi (glia) and 6X*Myc*-*SNCA*
680 (neurons). Note that α-Syn intensities significantly increases upon glial Aux depletion.
681 (**O**) A model illustrating Aux functions in glial autophagy. Aux regulates autophagic
682 induction, autophagosome biogenesis, and autolysosome maturation via Atg9
683 phosphorylation and trafficking. In the absence of glial Aux, Atg9 phosphorylation at
684 T62 and T69 is enhanced, promoting its trafficking to autophagosomes and lysosomes,
685 for function in the early and late stages of glial autophagy. Illustrations in blue represent
686 conditions under glial Aux depletion. Scale bars and the numbers of brains quantified
687 are indicated in the Figures. Data are shown as mean ± SEM. P-values of significance
688 (indicated with asterisks, ns no significance, * $p<0.05$, ** $p<0.01$, and *** $p<0.001$)
689 are calculated by two-tailed unpaired t-test or ordinary one-way ANOVA followed by
690 Tukey's multiple comparisons test.
691

692 **Materials and Methods**

693 ***Drosophila* genetics**

694 Flies were raised under standard conditions at 25°C with 70% humidity. All fly crosses
695 were carried out at 25°C with standard laboratory conditions unless noted otherwise.
696 All strains were obtained from Bloomington *Drosophila* Stock Center (BDSC), the
697 Vienna *Drosophila* RNAi Center (VDRC), Tsinghua Fly Center, or as gifts from
698 colleagues. MARCM clonal analyses were carried out using flies with the following
699 genotypes: *hs-FLP; UAS-mCherry.Atg8a* or *UAS-Lamp1.GFP;* FRT^{82B}*tub-*
700 $GAL80^{ts}$*/*FRT^{82B}*aux*. Flies were heat-shocked at 37°C for 30 minutes 4-5 days after
701 cross, then recovered at 25°C. 3- or 10-day-old adult fly brains were dissected. Detailed
702 fly genotypes for all experiments are listed in Key Resources Table.
703
704 **Mouse genetics**
705 The B6;129S6-$Gak^{tm2Legr}$/Mmjax mice (Cat. #36793-JAX, The Jackson laboratory, Bar
706 Harbor, ME, USA) possess loxP sites flanking exon 1 of *cyclin G associated kinase*
707 (*GAK*) gene. *CX3CR1-Cre* transgenic mice were kindly provided by Jiawei Zhou
708 (Institute of Neuroscience, Chinese Academy of Sciences). *CX3CR1-*$Cre^{+/-}$ littermates
709 were used as controls. Mice were housed in the animal facility with maximum of five
710 mice per cage under a 12 hours light/dark cycle at 22 ± 2°C. Food and water were
711 available *ad libitum*. The use and care of animals was approved and directed by the
712 Animal Care and Use Committee of National Center for Protein Science Shanghai.
713
714 **Cell line and transfections**

715 IMG cell line was a gift from Chih-Hao Lee (McCarthy et al., 2016). Cells were
716 cultured in Dulbecco's modified Eagle medium (Cat. #11965092, Gibco, New York,
717 NY, USA) with high glucose (4.5 g/L), 10 % fetal bovine serum (Cat. #10099141,
718 Gibco) and 100 units/mL penicillin-streptomycin (Cat. #15140-122, Gibco) at 37°C
719 with 5% CO2 humidified atmosphere. IMG cells were transfected using Lipo 2000 (Cat.
720 #11668019, Life Technologies, Carlsbad, CA, USA) according to the manufacturer's
721 protocol. In brief, cells were seeded on a 12-well plate overnight. 40 pmol siRNA
722 (GenePharma) and/or 2ul Lipo 2000 was diluted with 100 µl Opti-MEM (Cat.
723 #31985070, Gibco), mixed, and incubated at room temperature for 20 minutes, then
724 added dropwise to cells cultured at 37°C with 5% CO2. After 6 hours, cells were
725 changed into growth medium and harvested after 72 hours.
726
727 **Molecular biology**
728 Plasmid cloning: Plasmids were constructed by polymerase chain reaction (PCR) using
729 DNA templates from *Drosophila aux*, *atg9*, human *GAK*, and human *α-Syn*. These
730 plasmids express: Aux, Aux truncated variants including $Aux^{\Delta Kinase}$ (aa124-948),
731 $Aux^{\Delta PTEN}$ (aa1717-aa2121), $Aux^{\Delta CBD}$ (aa2542-3174), $Aux^{\Delta J}$ (aa3217-3441); Atg9,
732 EGFP-Atg9, Atg9 mutants including $Atg9^{T62A}$, $Atg9^{T69A}$, $Atg9^{T62A-T69A}$, $Atg9^{T62E}$,
733 $Atg9^{T69E}$, $Atg9^{T62E-T69E}$, human GAK; human α-Syn. The corresponding DNA
734 sequences were subcloned into *pUAST-attB* vector containing a 3XFlag or a 3XHA
735 epitope tag, *pJFRC19-13XLexAop2-attB* vector (Cat. #26224, Addgene, Watertown,

736 MA, USA) containing a 6XMyc epitope tag by Genscript (Nanjing, China). Fly
737 microinjection was conducted by the *Drosophila* Core Facility, Institute of
738 Biochemistry and Cell Biology, Chinese Academy of Sciences.
739 Primers used for amplification:
740 *aux*-F: CGCGGAATTCGGCGAGTTCTTTAAGTCGCTCAACCTCAAC
741 *aux*-R: CGCGCTCGAGTTACGCATTAAACATATTTTGCTGCGTGGC
742 *GAK*-F: CGGCCGCGAATTCATCGATAGATCTGATATCAACAAGTTTG
743 *GAK*-R:
744 GAAAGCTGGGTCGAATTCGCCCTTTCAGAAGAGGGGCCGGGAGCCCTG
745 *SNCA*-F: CCGGGCCTGGGATGTATTCATGAAAGGACTTTCAAAGG
746 *SNCA*-R: ACAAAGATCCTCTAGATTAGGCTTCAGG
747 qRT-PCR: Total RNAs were extracted from adult fly heads or IMG cells using
748 TransZol Up (Cat. #ET111-01, TransGen, Beijing, China). cDNAs were reversely
749 transcribed using HiScript III RT SuperMix (Cat. #R323-01, Vazyme, Nanjing, China).
750 qRT-PCR reactions were performed using ChamQ Universal SYBR qPCR Master Mix
751 (Cat. #Q711-02, Vazyme) and ABI 7500 RT-PCR system. The mRNA levels were
752 normalized to *rp49* (flies) or *Actin* (IMG cells), respectively. The expression levels
753 were analyzed by ΔΔCT method.
754 Primers used are listed below:
755 Flies:
756 *atg1*, *atg5*, *atg6*, *atg7*, *atg8a* as described previously (Yan et al., 2019).

757 *rp49*-F: CCACCAGTCGGATCGATATGC

758 *rp49*-R: CTCTTGAGAACGCAGGCGACC

759 *aux*-F: CAGCGGCTACCACCAATCCTTC

760 *aux*-R: TGCGTCGGCGTCCTGATAGA

761 *repo*-F: AAGTAGCAACAGCAGCCCAG

762 *repo*-R: CTTTTGCCACTGCGACACTT

763 *elav*-F: AGCATCCTGTTCCTGTGACG

764 *elav*-R: CGCGATTAGCGAGCTTTTGT

765 *atg9*-F: AGCAGAAGCACGGATTCACA

766 *atg9*-R: GCAGTGCATCACAAAGGCAA

767 IMG cells:

768 *Actin*-F: CTAAGGCCAACCGTGAAAAG

769 *Actin*-R: ACCAGAGGCATACAGGGACA

770 *GAK*-F: GGTCATCCAGTCTGTGGCTAAC

771 *GAK*-R: TTGATTGCAGACTCCACACC

772

773 **Immunohistochemistry**

774 Adult fly brains: Brains were dissected and fixed in 4% formaldehyde for 40 minutes,

775 then washed with PBT (PBS + 0.1% TX-100) for 3 times and dissected further to

776 remove additional debris in PBS solution. Clean and fixed brains were blocked in PBT

777 solution with 5% Normal Donkey Serum (NDS) and subsequently stained with primary

778 antibodies at 4°C overnight and then secondary antibodies at room temperature for 2
779 hours. Primary antibodies used: mouse anti-Atg8a (1:1000, gift from Chao Tong),
780 rabbit anti-Ref(2)P (1:500, Cat. #ab178440, Abcam, Cambridge, UK), mouse anti-
781 Mono- and polyubiquitinylated conjugates antibody (FK2, 1:500, Cat. #BML-PW8810,
782 Enzo Life Sciences, Farmingdale, NY, USA), rabbit anti-dATG9B (1:200, Cat.
783 #NB100-98679, Novus Biologicals, Littleton, CO, USA), mouse anti-Repo (1:100, Cat.
784 #8D12, Developmental Studies Hybridoma Bank, DSHB, Iowa City, IA, USA), rat
785 anti-Elav (1:500, Cat. #7E8A10, DSHB), and DDC (1:300, Jay Hirsh, primary).
786 IMG cells: Cells were seeded on glass coverslips in 12-well plates the day before
787 fixation with cold methanol (Cat. #100141190, Sinopharm, Beijing, China) for 15
788 minutes, followed by washing with PBT (PBS + 0.1% TX-100) for 15 minutes, then
789 blocked in PBS with 5% NDS for 1 hour. Cells were stained with primary antibodies at
790 4°C overnight and then secondary antibodies at room temperature for 2 hours. Primary
791 antibodies used: rabbit anti-Iba1 (1:500, Cat. #019-19741, Wako), rabbit anti-
792 TMEM119 (1:500, Cat. #ab185333, Abcam), rabbit anti-Lamp1 (1:400, Cat. #ab24170,
793 Abcam), rabbit anti-LC3B (1:200, Cat. #2775, Cell Signaling Technology, CST,
794 Danvers, MA, USA), and rabbit anti-GAK (1:50, Cat. #12147-1-AP, Proteintech,
795 Chicago, IL, USA). Nuclei were labeled by DAPI (Cat. #C1005, Beyotime, Shanghai,
796 China) at room temperature for 5-10 minutes.
797 Mouse brain slices: To prepare brain slices, mice were anesthetized with isoflurane and
798 perfused with 0.9% saline, followed by 4% paraformaldehyde in PBS. The brains were

799 removed and post-fixed overnight in 4% paraformaldehyde in PBS at 4°C. After
800 dehydration in 20% sucrose, a series of coronal sections (10 μm thick) across the
801 Substantia Nigra were cut by a Thermo CryoStar NX50 cryostat (Thermofisher
802 Scientific, USA). The sections were permeabilized with 0.3% Triton X-100 in PBS
803 containing 5% normal goat serum for 1 h at 37°C. After blocking with 5% normal goat
804 serum in PBS, the samples were incubated with primary antibodies at 4°C overnight.
805 Primary antibodies used: rabbit anti-TH (1:500, Cat. #AB152, Merck), rabbit anti-Iba-
806 1 (1:500, Cat. #019-19741, Wako), goat anti-Iba-1 (1:100, Cat. #ab5076, Abcam),
807 rabbit anti-GAK, and mouse anti-α-Synuclein (1:50, Cat. #sc-58480, Santa Cruz
808 Biotechnology). After three washes with 1XPBS, samples were incubated for 1 hour
809 with secondary antibodies conjugated with Alexa-fluorescein.

810 For all samples, secondary antibodies used were from Jackson ImmunoResearch
811 (West Grove, PA, USA): donkey anti-mouse Cy3 (1:1000, Cat. #715-166-151), donkey
812 anti-rabbit Cy3 (1:1000, Cat. #711-166-152), donkey anti-rat Cy3 (1:1000, Cat. #712-
813 165-153), donkey anti-mouse Cy5 (1:500, Cat. #715-175-150), donkey anti-rabbit Cy5
814 (1:500, Cat. #711-175-152) and donkey anti-rat Cy5 (1:500, Cat. #712-175-150). All
815 samples were mounted in Vectashield mounting media (Cat. #H-1500-10, Vector
816 Laboratories, Burlingame, CA, USA).

817

818 **LysoTracker staining**

819 Live adult fly brains were dissected in PBS, and immediately incubated in LysoTracker
820 Green DND-26 (1:1000, Cat. #L7526, Life technologies) solution with PBS (pre-
821 warmed at 37°C) for 5 minutes at 25°C. Images were taken by Nikon A1 microscope.
822 Live IMG cells were seeded on 8-well chamber slides overnight, and incubated in
823 LysoTracker solution (1:10000) with anti-fluorescence quenching DMEM (Cat.
824 #A1896701, Gibco). Images were taken by Nikon Spinning Disk at 37°C in 5% CO2.
825

826 **Cathepsin B detection with Magic Red**

827 Adult fly brains were dissected in PBS, and stained with 1× Magic Red Cathepsin B
828 dye for 10 min, according to the manufacturer's instruction (Magic Red® Cathepsin B
829 assay kits, Cat. #ICT937, BioRad). The red fluorescent intensities representing
830 cathepsin B activity in the cells were monitored under the Nikon A1 microscope.
831

832 ***In-vivo* time lapse analysis**

833 Live adult fly brains were dissected and kept in saline solution for tracing the GFP
834 puncta in a single focal plane using LSM 710 NLO (Zeiss, Germany) microscope with
835 a 20X water objective. The trafficking speed was analyzed by Imaris using Brownian
836 motion tracking mode.
837

838 **Transmission electron microscopy**

839 Adult fly brains were fixed, embedded, stained, and dehydrated according to previous
840 protocols (Li et al., 2013). Ultrathin sections (70 nm) of each brain were cut with a
841 Diatomediamond knife on a Leica EM UC7 ultra-microtome (Leica Microsystems,
842 Germany) and collected on copper grids. Images were acquired with Talos L120C
843 transmission electron microscope (Thermo Fisher Scientific, Waltham, MA, UAS)
844 operating at an acceleration voltage of 120 kV.
845
846 **Phosphorylomics**
847 Samples for phosphorylomic analysis were prepared and analyzed as described
848 previously (PTM Bio, Hangzhou, China (Yang et al., 2012)). 300 fly adult brains per
849 sample were sonicated three times on ice using a high intensity ultrasonic processor
850 (Scientz) in lysis buffer (8 M urea, 1% Protease Inhibitor Cocktail). For digestion, the
851 protein solution was reduced with 5 mM dithiothreitol for 30 mins at 56°C and alkylated
852 with 11 mM iodoacetamide for 15 mins at room temperature in darkness. The protein
853 sample was then diluted by adding 100 mM TEAB (tetraethylammonium bromide,
854 TEAB) to urea concentration less than 2 M. Finally, trypsin was added at 1:50 trypsin-
855 to-protein mass ratio for the first digestion overnight and 1:100 for a second 4 hour
856 digestion. After trypsin digestion, peptide was desalted by Strata X C18 SPE column
857 (Phenomenex) and vacuum-dried. Peptide was reconstituted in 0.5 M TEAB and
858 processed according to the manufacturer's protocol for TMT kit/iTRAQ kit. Briefly,
859 one unit of TMT/iTRAQ reagent were thawed and reconstituted in acetonitrile. The

860 peptide mixtures were then incubated for 2 h at room temperature and pooled, desalted
861 and dried by vacuum centrifugation. The tryptic peptides were dissolved in 0.1% formic
862 acid (solvent A), directly loaded onto a home-made reversed-phase analytical column
863 (15 cm length, 75 μm i.d.). The gradient was comprised of an increase from 6% to 23%
864 solvent B (0.1% formic acid in 98% acetonitrile) over 26 mins, 23% to 35% in 8 mins
865 and climbing to 80% in 3 mins then holding at 80% for the last 3 mins, all at a constant
866 flow rate of 400 nL/min on an EASY-nLC 1000 UPLC system. The peptides were
867 subjected to NSI source followed by tandem mass spectrometry (MS/MS) in Q
868 ExactiveTM Plus (Thermo) coupled online to the UPLC. The electrospray voltage
869 applied was 2.0 kV. The m/z scan range was 350 to 1800 for full scan, and intact
870 peptides were detected in the Orbitrap at a resolution of 70,000. Peptides were then
871 selected for MS/MS using NCE setting as 28 and the fragments were detected in the
872 Orbitrap at a resolution of 17,500. A data-dependent protocol that alternates between
873 one MS scan followed by 20 MS/MS scans with 15.0s dynamic exclusion was
874 conducted. Automatic gain control (AGC) was set at 5E4. Fixed first mass was set as
875 100 m/z.
876
877 **Biochemistry**
878 Western blot analysis: Fly adult heads were homogenised using a motorised pestle (Cat.
879 #116005500, MP Biomedicals, Irvine, CA, USA) in lysis buffer (0.4% NP-40, 0.2 mM
880 EDTA, 150 mM NaCl, 20% glycerol, 100 mM Tris-HCl pH7.5, 2% Tween 20, 0.5 mM

881 phosphodiesterase inhibitors, and 1 mM PMSF). Proteins were separated on SDS-
882 PAGE gels and transferred to PVDF membranes (Cat. #IPFL00010, Millipore, Billerica,
883 MA, USA). The membranes were blocked by 5% fat-free milk diluted in PBS with 0.1%
884 Tween-20 for 40 minutes. Samples were incubated with the primary antibodies at 4°C
885 overnight and HRP-conjugated secondary antibodies at room temperature for 2 hours.
886 Primary antibodies used: rat anti-Aux (1:1000, in this study), rabbit anti-
887 GABARAP+GABARAPL1+GABARAPL2 antibody (1:10000, Cat. #ab109364,
888 Abcam), rabbit anti-Ref(2)P (1:500, Cat. #ab178440, Abcam), mouse anti-Mono- and
889 polyubiquitinylated conjugates antibody (FK2, 1:500, Cat. #BML-PW8810, Enzo Life
890 Sciences), rabbit anti-dATG9B (1:200, Cat. #NB100-98679, Novus Biologicals), rabbit
891 anti-pS6K (1:1000, Cat. #9205S, Cell Signaling), rabbit anti-S6K (1:1000, Cat. #9202S,
892 Cell Signaling), rabbit anti-CathD (1:1000, Cat. #ab75852, Abcam), mouse anti-α-
893 Tubulin (1:5000, Cat. #T9026, Sigma), rabbit anti-Myc (1:2000, Cat. #0912-2,HuaAn
894 Biotechnology), mouse anti-α-Syn (1:1000, Cat. #180215, Invitrogen, Carlsbad, CA,
895 USA), and mouse anti-Flag (1:1000, Cat. #F3165, Sigma, St. Louis, MO, USA). Bands
896 were visualized by Clarity Western ECL Substrate (Cat. #WBKLS0500, Millipore).
897 Results are representative of at least three biological replicates. For IMG cells, cells
898 were treated and lysed in 2× SDS loading buffer at 95℃ for 10 minutes. Primary
899 antibodies used: rabbit anti-LC3B (1:200, Cat. #2775, CST), and rabbit anti-GAK (1:50,
900 Cat. #12147-1-AP, Proteintech), mouse anti-P62 (1:1000, Cat. #ab56416, Abcam) and
901 mouse anti-Ubiquitin (1:1000, Cat. #3936S, CST). For all examples, secondary

902 antibodies used are from Jackson ImmunoResearch: goat anti-mouse-HRP (1:5000, Cat.
903 #115-035-003), goat anti-rabbit-HRP (1:5000, Cat. #111-036-003) and goat anti-rat-
904 HRP (1:5000, Cat. #112-035-003).
905 BafilomycinA1 Treatment: BafA1 (Cat. #BML-CM110-0100, ENZO) was diluted in
906 DMSO (Cat. #D8371-50, solarbio) in a concentration of 1 mM, then added to 0.5 ml of
907 liquid yeast for a final concentration of 4 μM. Yeast containing BafA1 was added to
908 the top of the fly food in standard vials kept overnight to allow the evaporation of
909 residual DMSO. Flies of different genotypes (25 females and 25 males) were then put
910 in each vial and kept at 25°C for 5 days. After treatment, flies were collected for western
911 blot analysis.
912 anti-Aux antibodies: anti-Aux antibodies were generated by ABclonal Biotechnology
913 co., Ltd (Harrogate, UK). *aux* cDNA fragment encoding aa694-1157 was subcloned
914 into the pET-28a-SUMO vector, and purified proteins were injected into rats using
915 standard protocols to generate the antibodies.
916
917 **FACS analysis**
918 Adult fly brains were dissected in Schneider's medium (Cat. #21720024, Invitrogen)
919 and dissociated in 0.18 units/ml fresh papain (Cat. #LK003178, Worthington, Freehold,
920 NJ, USA) and 2.5mg/ml liberase TM (Cat. #5401119001, Roche, Basel, Switzerland)
921 with PBS. Approximately 100 or 400 brains were dissected for qRT-PCR or WB
922 analysis, respectively. Papain was activated at 37°C for 15 min before use. After

923 dissociation for 1 hour, cold Schneider's medium was added to inactivate the enzyme.
924 Samples were then filtered through cell strainer (Cat. #352340, BD Falcon, Franklin
925 Lakes, NJ, USA) into a flow cell tube (Cat. #352003, BD Falcon), centrifuged, and re-
926 suspended in the Schneider's medium. The suspension was then kept on ice and sent to
927 Flow cytometer (FACSMelody, BD). Fluorescent GFP or RFP signals were monitored
928 to sort adult fly glia. For transfected IMG cells, cells were harvested and filtered
929 through cell strainer as described above. Fluorescent Cy5 was used to sort IMG cells.
930

931 **Behavior analysis**

932 Mouse footprint gait analysis: To perform footprint gait analysis, mouse hindpaws and
933 forepaws were coated with black and red nontoxic paint, and trained to walk along a
934 33-cm long and 8-cm wide open-top runway (with 6.35-cm high walls). A fresh sheet
935 of white paper was placed on the floor of the runway for each run. The footprint patterns
936 were assessed quantitatively by stride length(Wertman et al., 2019).
937 Mouse pole test: Mice were placed with a 55-cm metal pole of 1-cm diameter covered
938 with adhesive tape to facilitate traction. Upon positioned head-up at the top of the pole,
939 the time required for mice to turn (t-turn) and climb down completely was recorded.
940 Fly lifespan analysis: The following fly strains were crossed to *repo-GAL4* and used
941 for lifespan analysis: isogenic w^{1118}, *UAS-LacZ*, *UAS-aux*-RNAi (V16182). These
942 strains were separately back-crossed to isogenic w^{1118} for five generations in order to
943 clean the genetic background before assessing longevity. Newly eclosed male or female

944 flies (1 to 2 days old; n=400 for each genotype) were collected and placed separately in
945 20 vials (each contains 20 unisex flies). Flies were transferred to new vials with
946 standard fly food every other days, and the number of dead flies were counted. All
947 experiments were repeated at least three times, and the percentage of flies survived
948 (live/total, %) was analyzed. Data points were drawn in curves using Prism software.
949 Fly locomotion analysis: The rapid iterative negative geotaxis (RING) assay was used
950 to analyze climbing ability as described previously(Cao et al., 2017; Gargano et al.,
951 2005; Song et al., 2017). Briefly, flies of different ages (3, 10, and 20 days old) were
952 collected and placed in vials with fly food (no yeast) for 1 day before transfering to the
953 cylinders for experiments. A total of 100 flies were analyzed in ten cylinders (inner
954 diameter: 20 mm; height: 200 mm) placed side by side, and each contains ten unisex
955 flies. An initial mechanical shock was applied for six times so that all flies were tapped
956 down to the bottom of the cylinder and synchronized. Climbing distances for each fly
957 were measured and averaged by RflyDetection software, which allows automatic
958 detection of fly position within the cylinder using video images captured every 6 s
959 (Sony digital camera, HDR-CX220E). At least three independent experiments were
960 performed. Data were shown as mean ± SEM.
961 Fly sleep analysis: The parental and F1 generation flies were raised on standard medium
962 in an incubator set to 25°C with 12 hour light/12 hour dark (LD) cycle. The flies were
963 collected at the age of 0-2 days old and mated for 2 days. Each mated female was then
964 loaded into sleep tubes (PGT5x65 Pyrex Glass, Trikinetics) that contained 2% agar and

965 5% sucrose at one end. The other end was sealed with parafilm with a hole for air-
966 circulation. The tubes were placed into the DAM2 *Drosophila* activity monitor system
967 (Trikinetics, Waltham) for sleep recording. Activity was recorded for five consecutive
968 days including entrainment for the first two days. Data from the following three days
969 were averaged for further analysis. The original data acquired by the DAM system
970 software were processed by DAMfileScan113. Sleep analysis was then performed
971 using an in-house program called SCAMP2019v2(Donelson et al., 2012) in Matlab
972 (MathWorks). Parameters of total sleep and sleep latency were calculated. Statistical
973 analyses were performed using GraphPad 8. Significance differences were determined
974 using Kruskal–Wallis tests for datasets that did not have a normal distribution and one-
975 way ANOVA for datasets normally distributed, followed by multiple comparisons tests.
976

977 **Confocal microscopy and statistical analysis**

978 Images of adult fly brains and IMG cells were acquired by scanning a serial Z-stack of
979 average 25-30 sections, each of 0.4 μm thickness, using Nikon A1, C2, or Spinning
980 Disk confocal microscope (Tokyo, Japan) with the 40X or 60X oil objective. The whole
981 brain was positioned so that they can be scanned anteriorly to posteriorly (top to
982 bottom). Super-resolution images were taken by STED SP8 (Zeiss, Germany) for a
983 single layer section on the desired regions using 100X oil objective. For statistical
984 analyses of number and size, original and unmodified images were imported into
985 ImageJ (National Institutes of Health), and the intensity threshold for the relevant

986 channel was set so that maximum number of dots were selected without miscounting
987 two adjacent dots into one. For colocalization measurements, primary images were
988 imported and analyzed automatically using the colocalization plugin with the intensity
989 correlation tool, showing as Pearson's correlation coefficient (R), Manders'
990 colocalization coefficients (tM1 or tM2), or the plot profile to show the mean radial
991 fluorescence. All data were imported into GraphPad Prism 8 and shown in scatter plots
992 or column bar graphs. For calculating the statistical significance, two-tailed unpaired t-
993 test or ordinary one-way ANOVA followed by Tukey's multiple comparisons test was
994 used. P value less than 0.05 is considered significant. ns: no significance, $p \geq 0.05$; *:
995 $p<0.05$; **: $p<0.01$; ***: $p<0.001$; ****: $p<0.0001$.
996

997 **References**

998 Bader, C.A., Shandala, T., Ng, Y.S., Johnson, I.R., and Brooks, D.A. (2015). Atg9 is
999 required for intraluminal vesicles in amphisomes and autolysosomes. Biol Open 4,
1000 1345-1355.
1001 Cao, W., Song, L., Cheng, J., Yi, N., Cai, L., Huang, F.D., and Ho, M. (2017). An
1002 Automated Rapid Iterative Negative Geotaxis Assay for Analyzing Adult Climbing
1003 Behavior in a Drosophila Model of Neurodegeneration. Journal of visualized
1004 experiments : JoVE.
1005 Cheng, J., Lu, Q., Song, L., and Ho, M.S. (2018). alpha-Synuclein Trafficking in
1006 Parkinson's Disease: Insights From Fly and Mouse Models. ASN Neuro 10,
1007 1759091418812587.
1008 Cheng, X.T., Zhou, B., Lin, M.Y., Cai, Q., and Sheng, Z.H. (2015). Axonal
1009 autophagosomes use the ride-on service for retrograde transport toward the soma.
1010 Autophagy 11, 1434-1436.
1011 Choi, I., Zhang, Y., Seegobin, S.P., Pruvost, M., Wang, Q., Purtell, K., Zhang, B., and
1012 Yue, Z. (2020). Microglia clear neuron-released alpha-synuclein via selective
1013 autophagy and prevent neurodegeneration. Nat Commun 11, 1386.
1014 Deng, Z., Purtell, K., Lachance, V., Wold, M.S., Chen, S., and Yue, Z. (2017).
1015 Autophagy Receptors and Neurodegenerative Diseases. Trends Cell Biol 27, 491-504.

1016 Dickson, D.W. (2012). Parkinson's disease and parkinsonism: neuropathology. Cold
1017 Spring Harb Perspect Med 2.
1018 Donelson, N.C., Kim, E.Z., Slawson, J.B., Vecsey, C.G., Huber, R., and Griffith, L.C.
1019 (2012). High-resolution positional tracking for long-term analysis of Drosophila sleep
1020 and locomotion using the "tracker" program. PLoS One 7, e37250.
1021 Feng, Y., Backues, S.K., Baba, M., Heo, J.M., Harper, J.W., and Klionsky, D.J.
1022 (2016). Phosphorylation of Atg9 regulates movement to the phagophore assembly site
1023 and the rate of autophagosome formation. Autophagy 12, 648-658.
1024 Filippini, A., Gennarelli, M., and Russo, I. (2019). alpha-Synuclein and Glia in
1025 Parkinson's Disease: A Beneficial or a Detrimental Duet for the Endo-Lysosomal
1026 System? Cell Mol Neurobiol 39, 161-168.
1027 Galluzzi, L., Baehrecke, E.H., Ballabio, A., Boya, P., Bravo-San Pedro, J.M., Cecconi,
1028 F., Choi, A.M., Chu, C.T., Codogno, P., Colombo, M.I., *et al.* (2017). Molecular
1029 definitions of autophagy and related processes. EMBO J 36, 1811-1836.
1030 Gargano, J.W., Martin, I., Bhandari, P., and Grotewiel, M.S. (2005). Rapid iterative
1031 negative geotaxis (RING): a new method for assessing age-related locomotor decline
1032 in Drosophila. Experimental gerontology 40, 386-395.
1033 Gleichman, A.J., and Carmichael, S.T. (2020). Glia in neurodegeneration: Drivers of
1034 disease or along for the ride? Neurobiol Dis 142, 104957.
1035 Hara, T., Nakamura, K., Matsui, M., Yamamoto, A., Nakahara, Y., Suzuki-Migishima,
1036 R., Yokoyama, M., Mishima, K., Saito, I., Okano, H., and Mizushima, N. (2006).
1037 Suppression of basal autophagy in neural cells causes neurodegenerative disease in
1038 mice. Nature 441, 885-889.
1039 He, K., Song, E., Upadhyayula, S., Dang, S., Gaudin, R., Skillern, W., Bu, K.,
1040 Capraro, B.R., Rapoport, I., Kusters, I., *et al.* (2020). Dynamics of Auxilin 1 and
1041 GAK in clathrin-mediated traffic. J Cell Biol 219.
1042 Hegedus, K., Takats, S., Kovacs, A.L., and Juhasz, G. (2013). Evolutionarily
1043 conserved role and physiological relevance of a STX17/Syx17 (syntaxin 17)-
1044 containing SNARE complex in autophagosome fusion with endosomes and
1045 lysosomes. Autophagy 9, 1642-1646.
1046 Ho, M.S. (2019). Microglia in Parkinson's Disease. Adv Exp Med Biol 1175, 335-
1047 353.
1048 Jellinger, K.A. (2018). Multiple System Atrophy: An Oligodendroglioneural
1049 Synucleinopathy1. J Alzheimers Dis 62, 1141-1179.
1050 Kim, J., Kundu, M., Viollet, B., and Guan, K.L. (2011). AMPK and mTOR regulate
1051 autophagy through direct phosphorylation of Ulk1. Nat Cell Biol 13, 132-141.
1052 Klionsky, D.J., Abdelmohsen, K., Abe, A., Abedin, M.J., Abeliovich, H., Acevedo
1053 Arozena, A., Adachi, H., Adams, C.M., Adams, P.D., Adeli, K., *et al.* (2016).
1054 Guidelines for the use and interpretation of assays for monitoring autophagy (3rd
1055 edition). Autophagy 12, 1-222.
1056 Komatsu, M., Waguri, S., Chiba, T., Murata, S., Iwata, J., Tanida, I., Ueno, T., Koike,
1057 M., Uchiyama, Y., Kominami, E., and Tanaka, K. (2006). Loss of autophagy in the

1058 central nervous system causes neurodegeneration in mice. Nature 441, 880-884.
1059 Kulkarni, A., Chen, J., and Maday, S. (2018). Neuronal autophagy and intercellular
1060 regulation of homeostasis in the brain. Curr Opin Neurobiol 51, 29-36.
1061 Lee, D.W., Wu, X., Eisenberg, E., and Greene, L.E. (2006). Recruitment dynamics of
1062 GAK and auxilin to clathrin-coated pits during endocytosis. J Cell Sci 119, 3502-
1063 3512.
1064 Levine, B., and Kroemer, G. (2019). Biological Functions of Autophagy Genes: A
1065 Disease Perspective. Cell 176, 11-42.
1066 Li, H., Li, Y., Lei, Z., Wang, K., and Guo, A. (2013). Transformation of odor
1067 selectivity from projection neurons to single mushroom body neurons mapped with
1068 dual-color calcium imaging. Proc Natl Acad Sci U S A 110, 12084-12089.
1069 Maday, S., Wallace, K.E., and Holzbaur, E.L. (2012). Autophagosomes initiate
1070 distally and mature during transport toward the cell soma in primary neurons. J Cell
1071 Biol 196, 407-417.
1072 Mari, M., Griffith, J., Rieter, E., Krishnappa, L., Klionsky, D.J., and Reggiori, F.
1073 (2010). An Atg9-containing compartment that functions in the early steps of
1074 autophagosome biogenesis. J Cell Biol 190, 1005-1022.
1075 Mauvezin, C., Nagy, P., Juhasz, G., and Neufeld, T.P. (2015). Autophagosome-
1076 lysosome fusion is independent of V-ATPase-mediated acidification. Nat Commun 6,
1077 7007.
1078 McCarthy, R.C., Lu, D.Y., Alkhateeb, A., Gardeck, A.M., Lee, C.H., and Wessling-
1079 Resnick, M. (2016). Characterization of a novel adult murine immortalized microglial
1080 cell line and its activation by amyloid-beta. J Neuroinflammation 13, 21.
1081 Menzies, F.M., Fleming, A., Caricasole, A., Bento, C.F., Andrews, S.P., Ashkenazi, A.,
1082 Fullgrabe, J., Jackson, A., Jimenez Sanchez, M., Karabiyik, C., *et al.* (2017).
1083 Autophagy and Neurodegeneration: Pathogenic Mechanisms and Therapeutic
1084 Opportunities. Neuron 93, 1015-1034.
1085 Mizushima, N. (2020). The ATG conjugation systems in autophagy. Curr Opin Cell
1086 Biol 63, 1-10.
1087 Nixon, R.A. (2013). The role of autophagy in neurodegenerative disease. Nat Med 19,
1088 983-997.
1089 Orsi, A., Razi, M., Dooley, H.C., Robinson, D., Weston, A.E., Collinson, L.M., and
1090 Tooze, S.A. (2012). Dynamic and transient interactions of Atg9 with autophagosomes,
1091 but not membrane integration, are required for autophagy. Mol Biol Cell 23, 1860-
1092 1873.
1093 Papinski, D., Schuschnig, M., Reiter, W., Wilhelm, L., Barnes, C.A., Maiolica, A.,
1094 Hansmann, I., Pfaffenwimmer, T., Kijanska, M., Stoffel, I., *et al.* (2014). Early steps
1095 in autophagy depend on direct phosphorylation of Atg9 by the Atg1 kinase. Mol Cell
1096 53, 471-483.
1097 Peng, C., Trojanowski, J.Q., and Lee, V.M. (2020). Protein transmission in
1098 neurodegenerative disease. Nat Rev Neurol 16, 199-212.
1099 Puri, C., Renna, M., Bento, C.F., Moreau, K., and Rubinsztein, D.C. (2013). Diverse

1100 autophagosome membrane sources coalesce in recycling endosomes. Cell 154, 1285-
1101 1299.
1102 Puri, C., Renna, M., Bento, C.F., Moreau, K., and Rubinsztein, D.C. (2014).
1103 ATG16L1 meets ATG9 in recycling endosomes: additional roles for the plasma
1104 membrane and endocytosis in autophagosome biogenesis. Autophagy 10, 182-184.
1105 Ravikumar, B., Moreau, K., Jahreiss, L., Puri, C., and Rubinsztein, D.C. (2010).
1106 Plasma membrane contributes to the formation of pre-autophagosomal structures. Nat
1107 Cell Biol 12, 747-757.
1108 Russell, R.C., Tian, Y., Yuan, H., Park, H.W., Chang, Y.Y., Kim, J., Kim, H., Neufeld,
1109 T.P., Dillin, A., and Guan, K.L. (2013). ULK1 induces autophagy by phosphorylating
1110 Beclin-1 and activating VPS34 lipid kinase. Nat Cell Biol 15, 741-750.
1111 Shimizu, H., Nagamori, I., Yabuta, N., and Nojima, H. (2009). GAK, a regulator of
1112 clathrin-mediated membrane traffic, also controls centrosome integrity and
1113 chromosome congression. J Cell Sci 122, 3145-3152.
1114 Simonsen, A., Cumming, R.C., Brech, A., Isakson, P., Schubert, D.R., and Finley,
1115 K.D. (2008). Promoting basal levels of autophagy in the nervous system enhances
1116 longevity and oxidant resistance in adult Drosophila. Autophagy 4, 176-184.
1117 Song, L., He, Y., Ou, J., Zhao, Y., Li, R., Cheng, J., Lin, C.H., and Ho, M.S. (2017).
1118 Auxilin Underlies Progressive Locomotor Deficits and Dopaminergic Neuron Loss in
1119 a Drosophila Model of Parkinson's Disease. Cell Rep 18, 1132-1143.
1120 Sorrentino, Z.A., Giasson, B.I., and Chakrabarty, P. (2019). alpha-Synuclein and
1121 astrocytes: tracing the pathways from homeostasis to neurodegeneration in Lewy
1122 body disease. Acta Neuropathol 138, 1-21.
1123 Subhramanyam, C.S., Wang, C., Hu, Q., and Dheen, S.T. (2019). Microglia-mediated
1124 neuroinflammation in neurodegenerative diseases. Semin Cell Dev Biol 94, 112-120.
1125 Tanriover, G., Bacioglu, M., Schweighauser, M., Mahler, J., Wegenast-Braun, B.M.,
1126 Skodras, A., Obermuller, U., Barth, M., Kronenberg-Versteeg, D., Nilsson, K.P.R., *et*
1127 *al.* (2020). Prominent microglial inclusions in transgenic mouse models of alpha-
1128 synucleinopathy that are distinct from neuronal lesions. Acta Neuropathol Commun 8,
1129 133.
1130 Valdinocci, D., Radford, R.A., Siow, S.M., Chung, R.S., and Pountney, D.L. (2017).
1131 Potential Modes of Intercellular alpha-Synuclein Transmission. Int J Mol Sci 18.
1132 Wertman, V., Gromova, A., La Spada, A.R., and Cortes, C.J. (2019). Low-Cost Gait
1133 Analysis for Behavioral Phenotyping of Mouse Models of Neuromuscular Disease.
1134 Journal of visualized experiments : JoVE.
1135 Xu, Q., Bernardo, A., Walker, D., Kanegawa, T., Mahley, R.W., and Huang, Y. (2006).
1136 Profile and regulation of apolipoprotein E (ApoE) expression in the CNS in mice with
1137 targeting of green fluorescent protein gene to the ApoE locus. J Neurosci 26, 4985-
1138 4994.
1139 Yamamoto, H., Kakuta, S., Watanabe, T.M., Kitamura, A., Sekito, T., Kondo-Kakuta,
1140 C., Ichikawa, R., Kinjo, M., and Ohsumi, Y. (2012). Atg9 vesicles are an important
1141 membrane source during early steps of autophagosome formation. J Cell Biol 198,

1142 219-233.
1143 Yan, C., Liu, J., Gao, J., Sun, Y., Zhang, L., Song, H., Xue, L., Zhan, L., Gao, G., Ke,
1144 Z., *et al.* (2019). IRE1 promotes neurodegeneration through autophagy-dependent
1145 neuron death in the Drosophila model of Parkinson's disease. Cell Death Dis 10, 800.
1146 Yang, Q.S., Wu, J.H., Li, C.Y., Wei, Y.R., Sheng, O., Hu, C.H., Kuang, R.B., Huang,
1147 Y.H., Peng, X.X., McCardle, J.A., *et al.* (2012). Quantitative proteomic analysis
1148 reveals that antioxidation mechanisms contribute to cold tolerance in plantain (Musa
1149 paradisiaca L.; ABB Group) seedlings. Molecular & cellular proteomics : MCP 11,
1150 1853-1869.
1151 Yoshimori, T., Yamamoto, A., Moriyama, Y., Futai, M., and Tashiro, Y. (1991).
1152 Bafilomycin A1, a specific inhibitor of vacuolar-type H(+)-ATPase, inhibits
1153 acidification and protein degradation in lysosomes of cultured cells. J Biol Chem 266,
1154 17707-17712.
1155 Zhang, C.X., Engqvist-Goldstein, A.E., Carreno, S., Owen, D.J., Smythe, E., and
1156 Drubin, D.G. (2005). Multiple roles for cyclin G-associated kinase in clathrin-
1157 mediated sorting events. Traffic 6, 1103-1113.
1158 Zhang, Y., Chen, K., Sloan, S.A., Bennett, M.L., Scholze, A.R., O'Keeffe, S.,
1159 Phatnani, H.P., Guarnieri, P., Caneda, C., Ruderisch, N., *et al.* (2014). An RNA-
1160 sequencing transcriptome and splicing database of glia, neurons, and vascular cells of
1161 the cerebral cortex. J Neurosci 34, 11929-11947.
1162 Zhang, Y., Sloan, S.A., Clarke, L.E., Caneda, C., Plaza, C.A., Blumenthal, P.D.,
1163 Vogel, H., Steinberg, G.K., Edwards, M.S., Li, G., *et al.* (2016). Purification and
1164 Characterization of Progenitor and Mature Human Astrocytes Reveals Transcriptional
1165 and Functional Differences with Mouse. Neuron 89, 37-53.
1166 Zhou, C., Ma, K., Gao, R., Mu, C., Chen, L., Liu, Q., Luo, Q., Feng, D., Zhu, Y., and
1167 Chen, Q. (2017). Regulation of mATG9 trafficking by Src- and ULK1-mediated
1168 phosphorylation in basal and starvation-induced autophagy. Cell Res 27, 184-201.

1169

Figure 1

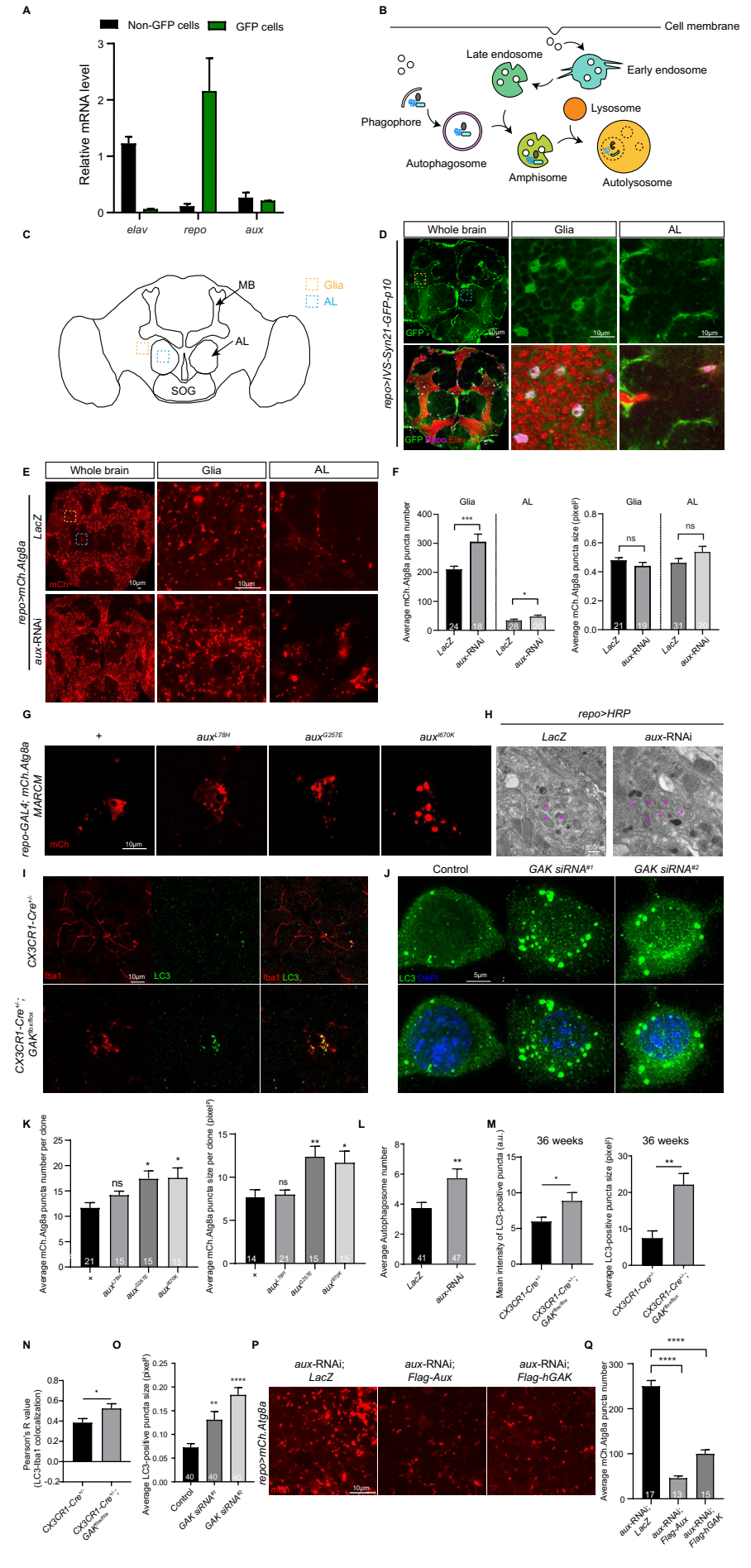
A
Non-GFP cells
GFP cells
Relative mRNA level
elav
repo
aux
B
Cell membrane
Late endosome
Early endosome
Lysosome
Phagophore
Autophagosome
Amphisome
Autolysosome
C
MB
Glia
AL
AL
SOG
D
Whole brain
Glia
AL
repo>IVS-Syn21-GFP-p10
GFP
GFP Repo Elav
10µm
E
Whole brain
Glia
AL
repo>mCh.Atg8a
LacZ
aux-RNAi
mCh
10µm
F
Glia
AL
Average mCh.Atg8a puncta number
Average mCh.Atg8a puncta size (pixel²)
***
*
ns
ns
LacZ
aux-RNAi
24
18
28
20
21
19
31
27
G
+
auxL78H
auxG257E
auxI670K
repo-GAL4; mCh.Atg8a MARCM
mCh
10µm
H
repo>HRP
LacZ
aux-RNAi
500nm
I
CX3CR1-Cre+/-
CX3CR1-Cre+/-; GAKfl/flflox
Iba1
LC3
10µm
J
Control
GAK siRNA#1
GAK siRNA#2
LC3 DAPI
5µm
K
Average mCh.Atg8a puncta number per clone
Average mCh.Atg8a puncta size per clone (pixel²)
ns
ns
*
*
**
*
21
15
15
15
14
21
15
15
L
Average Autophagosome number
**
LacZ
aux-RNAi
41
47
M
36 weeks
Mean intensity of LC3-positive puncta (a.u.)
36 weeks
Average LC3-positive puncta size (pixel²)
*
**
CX3CR1-Cre+/-
CX3CR1-Cre+/-; GAKfl/flflox
N
Pearson's R value (LC3-Iba1 colocalization)
*
CX3CR1-Cre+/-
CX3CR1-Cre+/-; GAKfl/flflox
O
Average LC3-positive puncta size (pixel²)
**
****
Control
GAK siRNA#1
GAK siRNA#2
40
40
P
aux-RNAi; LacZ
aux-RNAi; Flag-Aux
aux-RNAi; Flag-hGAK
repo>mCh.Atg8a
mCh
10µm
Q
Average mCh.Atg8a puncta number
****
****
17
13
15
aux-RNAi; LacZ
aux-RNAi; Flag-Aux
aux-RNAi; Flag-hGAK

Figure 2

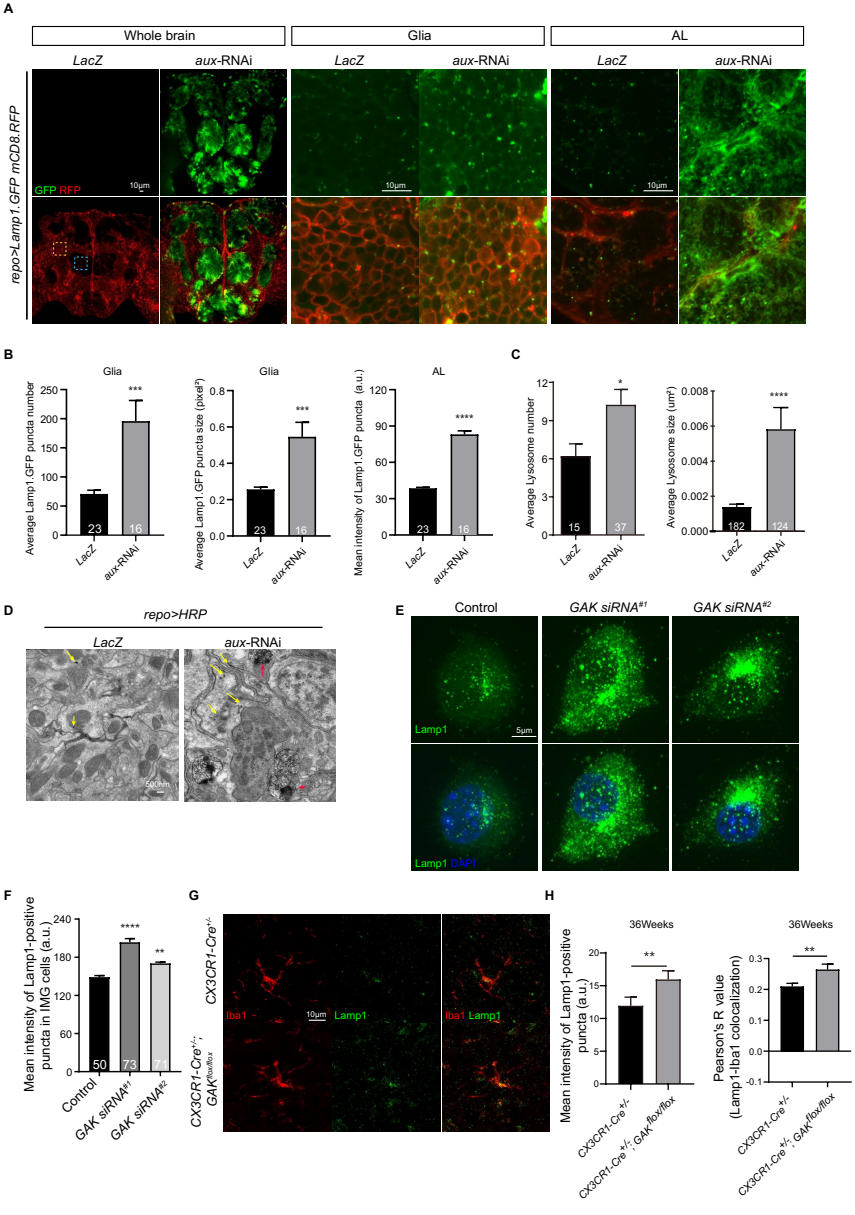
A
Whole brain
Glia
AL
LacZ
aux-RNAi
repo>Lamp1.GFP mCD8.RFP
GFP RFP
10μm
B
Glia
AL
Average Lamp1.GFP puncta number
Average Lamp1.GFP puncta size (pixel²)
Mean intensity of Lamp1.GFP puncta (a.u.)
C
Average Lysosome number
Average Lysosome size (um²)
D
repo>HRP
5μm
E
Control
GAK siRNA#1
GAK siRNA#2
Lamp1
Lamp1 DAPI
5μm
F
Mean intensity of Lamp1-positive puncta in IMG cells (a.u.)
Control
GAK siRNA#1
GAK siRNA#2
G
CX3CR1-Cre+/-
CX3CR1-Cre+/-; GAKflox/flox
Iba1
Lamp1
10μm
H
36Weeks
Mean intensity of Lamp1-positive puncta (a.u.)
Pearson's R value (Lamp1-Iba1 colocalization)
CX3CR1-Cre+/-
CX3CR1-Cre+/-; GAKflox/flox

Figure 3

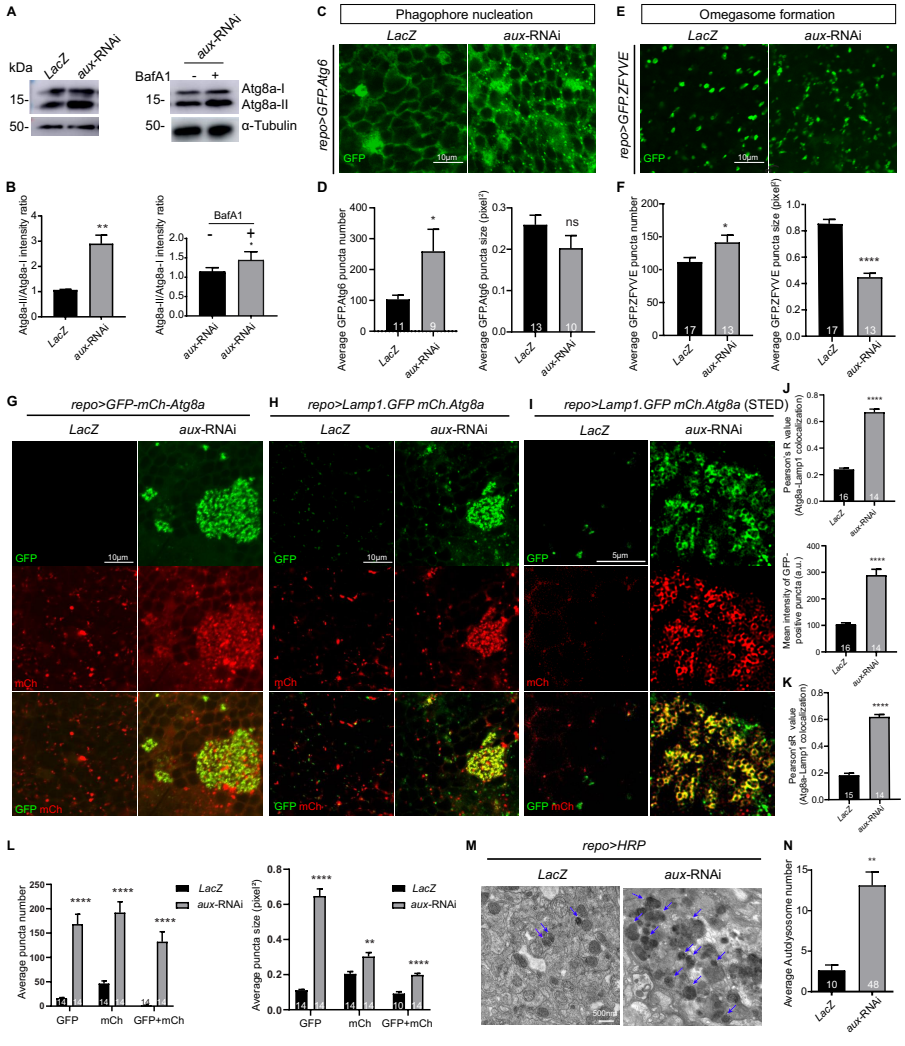
A
kDa
LacZ
aux-RNAi
15-
50-
BafA1
-
+
Atg8a-I
Atg8a-II
α-Tubulin
B
Atg8a-II/Atg8a-I intensity ratio
**
BafA1
C
Phagophore nucleation
repo>GFP.Atg6
GFP
10μm
D
Average GFPAtg6 puncta number
Average GFPAtg6 puncta size (pixel²)
ns
E
Omegasome formation
repo>GFP.ZFYVE
F
Average GFPZFYVE puncta number
Average GFPZFYVE puncta size (pixel²)
****
G
repo>GFP-mCh-Atg8a
mCh
GFP mCh
H
repo>Lamp1.GFP mCh.Atg8a
I
repo>Lamp1.GFP mCh.Atg8a (STED)
5μm
J
Pearson's R value (Atg8a-Lamp1 colocalization)
Mean intensity of GFP-positive puncta (a.u.)
K
Pearson's R value (Atg8a-Lamp1 colocalization)
L
Average puncta number
Average puncta size (pixel²)
GFP
mCh
GFP+mCh
M
repo>HRP
500nm
N
Average Autolysosome number

Figure 4

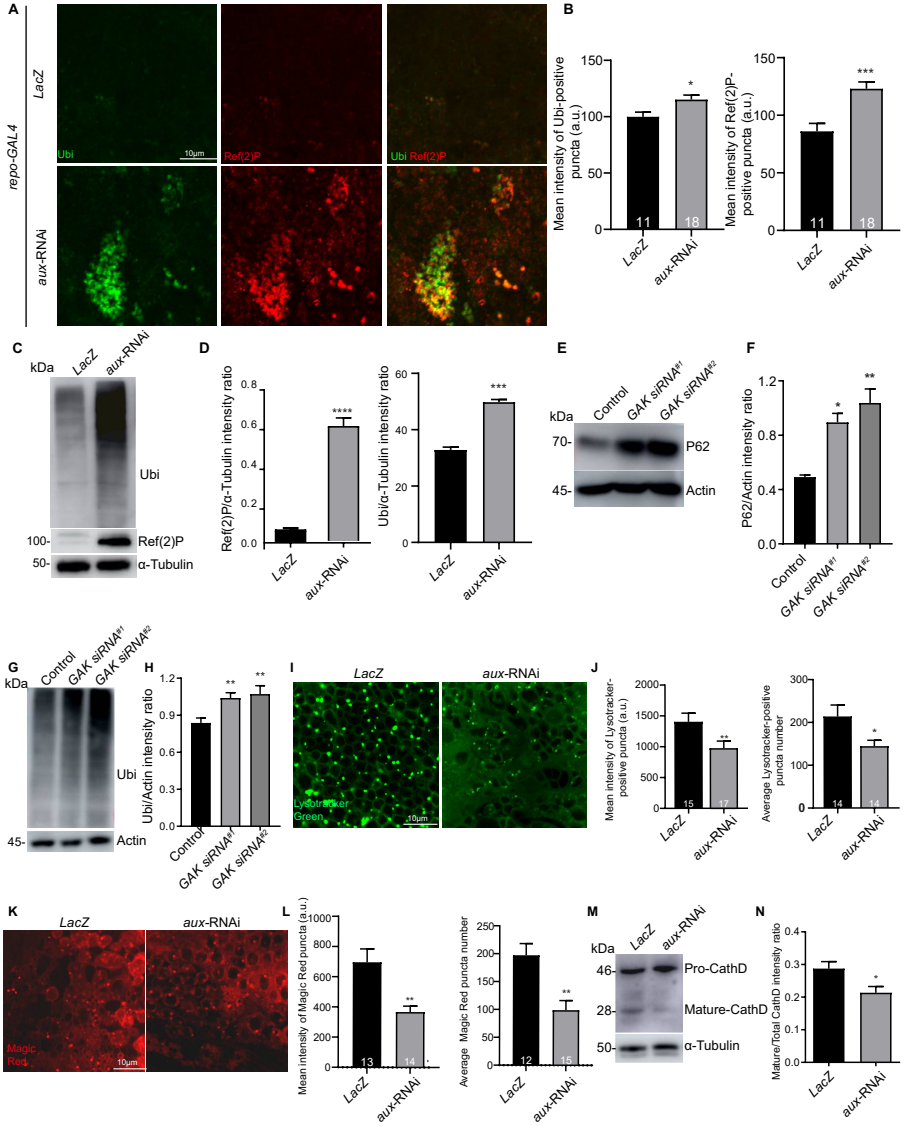
A
repo-GAL4
LacZ
aux-RNAi
Ubi
Ref(2)P
Ubi Ref(2)P
10μm
B
Mean intensity of Ubi-positive puncta (a.u.)
Mean intensity of Ref(2)P-positive puncta (a.u.)
LacZ
aux-RNAi
C
kDa
Ubi
Ref(2)P
α-Tubulin
D
Ref(2)P/α-Tubulin intensity ratio
Ubi/α-Tubulin intensity ratio
E
Control
GAK siRNA#1
GAK siRNA#2
P62
Actin
F
P62/Actin intensity ratio
G
H
Ubi/Actin intensity ratio
I
Lysotracker Green
J
Mean intensity of Lysotracker-positive puncta (a.u.)
Average Lysotracker-positive puncta number
K
Magic Red
L
Mean intensity of Magic Red puncta (a.u.)
Average Magic Red puncta number
M
Pro-CathD
Mature-CathD
N
Mature/Total CathD intensity ratio

Figure 5

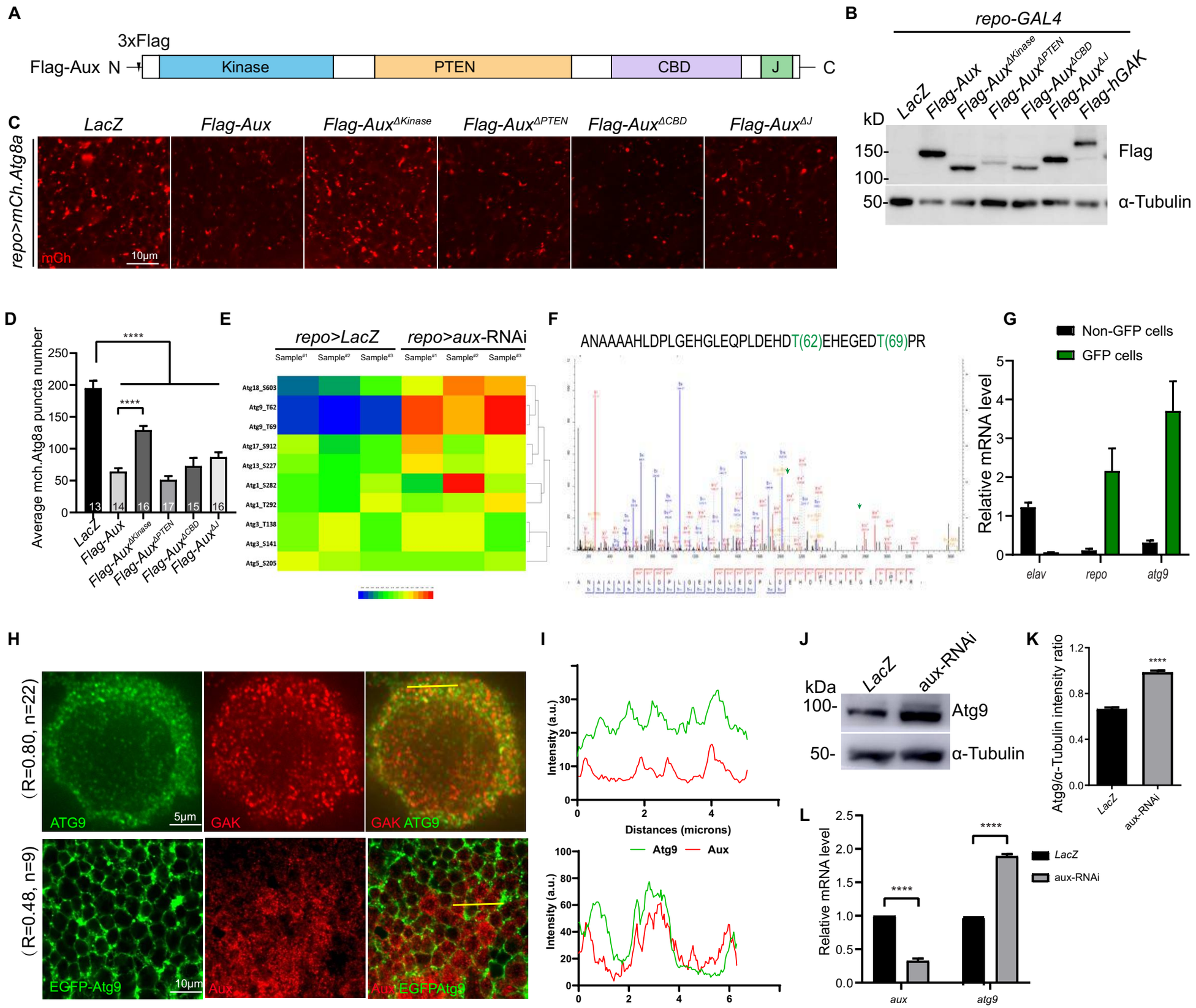
A
3xFlag
Flag-Aux N
Kinase
PTEN
CBD
J
C
B
repo-GAL4
LacZ
Flag-Aux
Flag-AuxΔKinase
Flag-AuxΔPTEN
Flag-AuxΔCBD
Flag-AuxΔJ
Flag-hGAK
kD
150-
100-
50-
Flag
α-Tubulin
C
repo>mCh.Atg8a
mCh
10μm
D
Average mch.Atg8a puncta number
****
13
14
16
17
15
16
E
repo>LacZ
repo>aux-RNAi
Sample#1
Sample#2
Sample#3
Atg18_S603
Atg9_T62
Atg9_T69
Atg17_S912
Atg13_S227
Atg1_S282
Atg1_T292
Atg3_T138
Atg3_S141
Atg5_S205
F
ANAAAAHLDPLGEHGLEQPLDEHDT(62)EHEGEDT(69)PR
G
Non-GFP cells
GFP cells
Relative mRNA level
elav
repo
atg9
H
(R=0.80, n=22)
ATG9
5μm
GAK
GAK ATG9
(R=0.48, n=9)
EGFP-Atg9
10μm
Aux
Aux EGFPAtg9
I
Intensity (a.u.)
Distances (microns)
Atg9
Aux
J
LacZ
aux-RNAi
kDa
100-
50-
Atg9
α-Tubulin
K
Atg9/α-Tubulin intensity ratio
L
Relative mRNA level
LacZ
aux-RNAi
aux
atg9

Figure 6

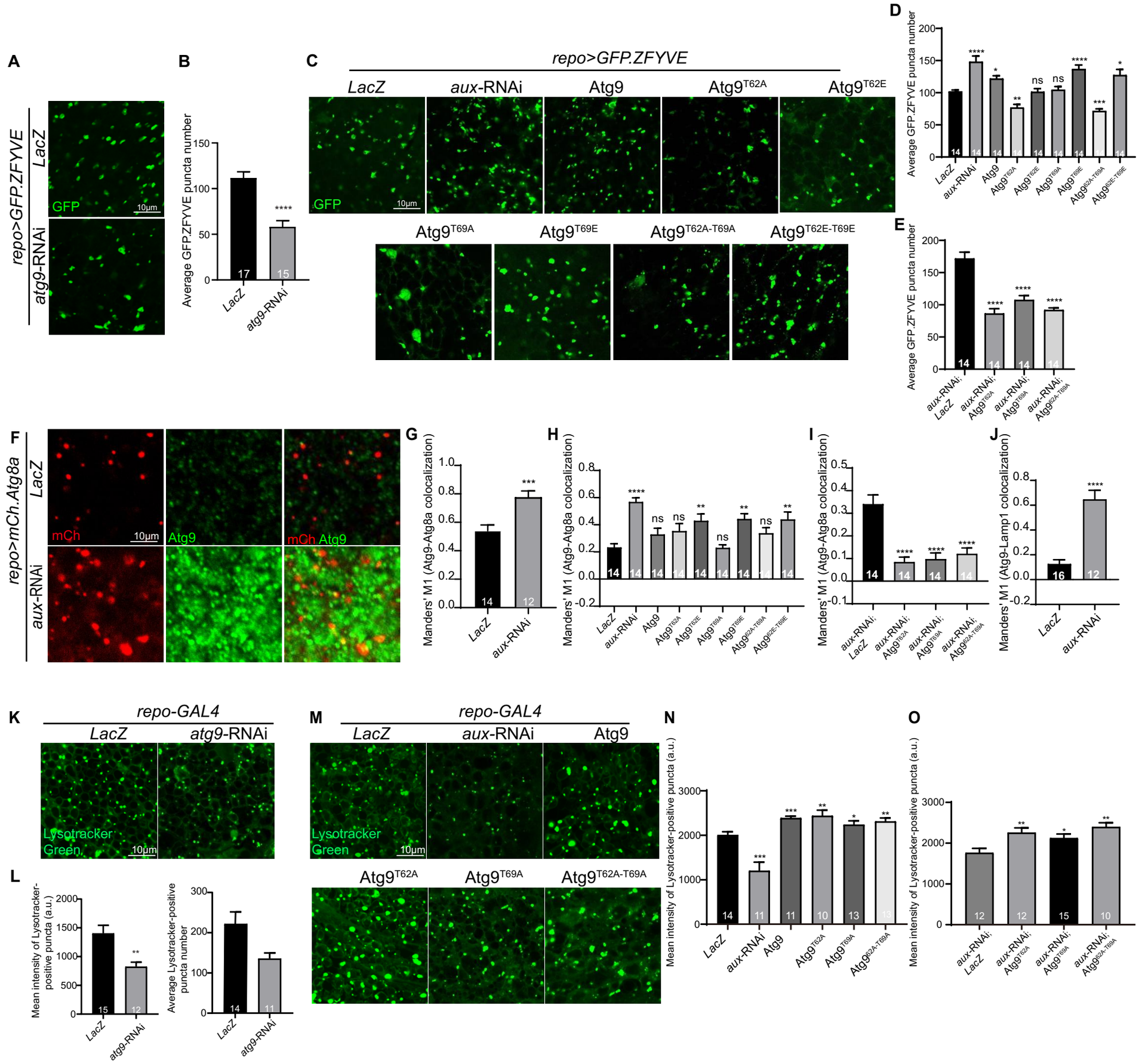
A
repo>GFP.ZFYVE
LacZ
atg9-RNAi
GFP
10µm
B
Average GFP.ZFYVE puncta number
****
17
15
LacZ
atg9-RNAi
C
repo>GFP.ZFYVE
LacZ
aux-RNAi
Atg9
Atg9T62A
Atg9T62E
Atg9T69A
Atg9T69E
Atg9T62A-T69A
Atg9T62E-T69E
D
Average GFP.ZFYVE puncta number
E
aux-RNAi; LacZ
aux-RNAi; Atg9T62A
aux-RNAi; Atg9T69A
aux-RNAi; Atg9T62A-T69A
F
repo>mCh.Atg8a
mCh
Atg9
mCh Atg9
G
Manders' M1 (Atg9-Atg8a colocalization)
H
I
J
Manders' M1 (Atg9-Lamp1 colocalization)
K
repo-GAL4
Lysotracker Green
L
Mean intensity of Lysotracker-positive puncta (a.u.)
Average Lysotracker-positive puncta number
M
N
O

Figure 7

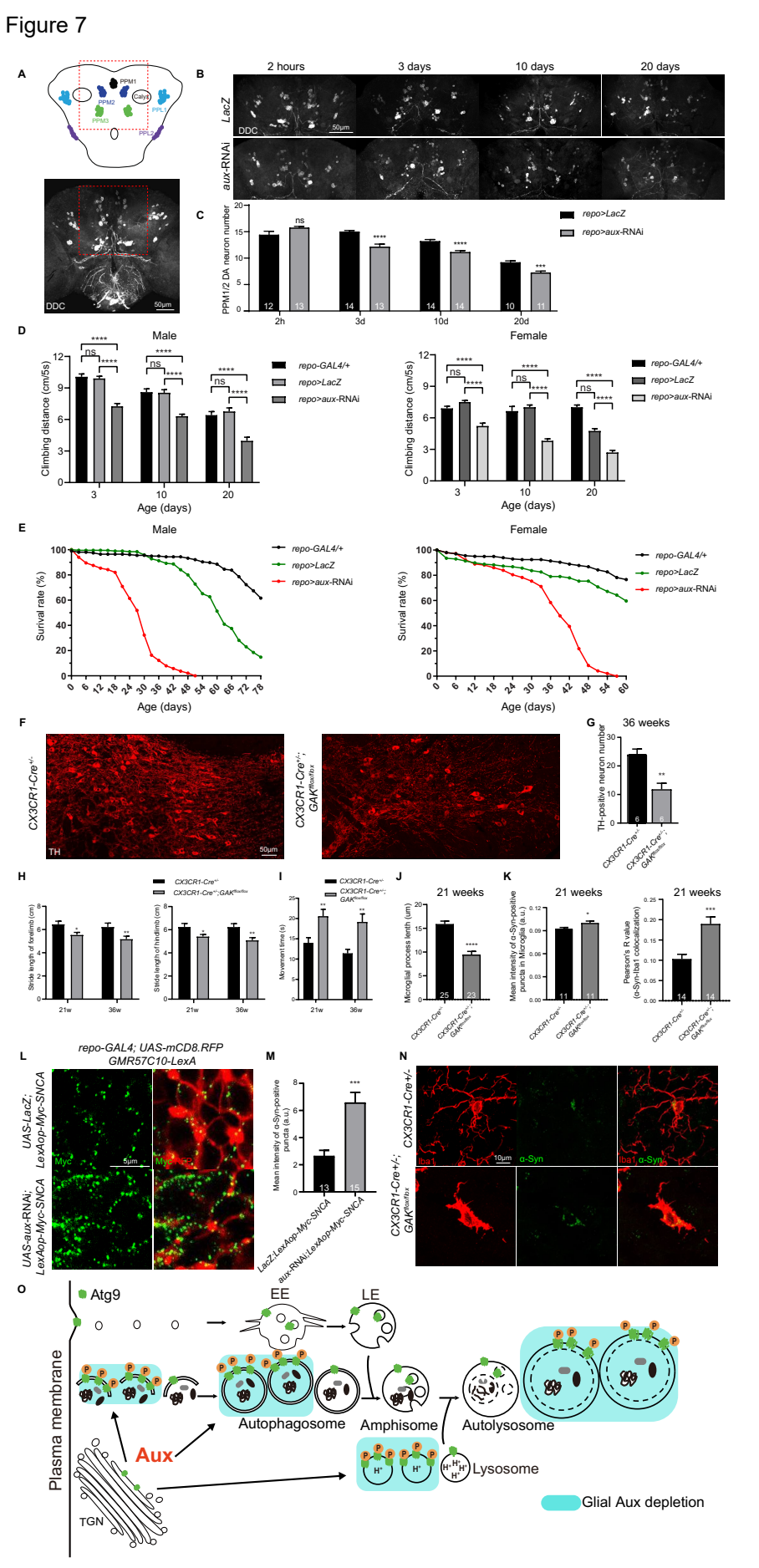

A
PPM1
PPM2
PPM3
PPL1
PPL2
Calyx
DDC
50μm
B
2 hours
3 days
10 days
20 days
LacZ
aux-RNAi
DDC
50μm
C
PPM1/2 DA neuron number
repo>LacZ
repo>aux-RNAi
ns
2h
3d
10d
20d
D
Male
Female
Climbing distance (cm/5s)
Age (days)
repo-GAL4/+
repo>LacZ
repo>aux-RNAi
E
Male
Female
Surival rate (%)
Age (days)
repo-GAL4/+
repo>LacZ
repo>aux-RNAi
F
CX3CR1-Cre+/-
CX3CR1-Cre+/-; GAKflox/flox
TH
50μm
G
36 weeks
TH-positive neuron number
H
Stride length of forelimb (cm)
Stride length of hindlimb (cm)
21w
36w
I
Movement time (s)
21w
36w
J
21 weeks
Microglial process lenth (um)
K
21 weeks
Mean intensity of α-Syn-positive puncta in Microglia (a.u.)
21 weeks
Pearson's R value (α-Syn-Iba1 colocalization)
L
repo-GAL4; UAS-mCD8.RFP
GMR57C10-LexA
UAS-LacZ; LexAop-Myc-SNCA
UAS-aux-RNAi; LexAop-Myc-SNCA
Myc
Myc-NRP
5μm
M
Mean intensity of α-Syn-positive puncta (a.u.)
LacZ;LexAop-Myc-SNCA
aux-RNAi;LexAop-Myc-SNCA
N
CX3CR1-Cre+/-
CX3CR1-Cre+/-; GAKflox/flox
Iba1
α-Syn
10μm
O
Atg9
EE
LE
Plasma membrane
Autophagosome
Amphisome
Autolysosome
Aux
Lysosome
TGN
Glial Aux depletion